NEUROSCIENCE

# Somatosensory cortical signature of facial nociception and vibrotactile touch–induced analgesia

**Jinghao Lu[1,2]†*, Bin Chen[1]†, Manuel Levy[1], Peng Xu[3], Bao-Xia Han[2], Jun Takatoh[1], P. M. Thompson[1], Zhigang He[4], Vincent Prevosto[1], Fan Wang[1,2]***



**Pain relief by vibrotactile touch is a common human experience. Previous neurophysiological investigations of its underlying mechanism in animals focused on spinal circuits, while human studies suggested the involvement of supraspinal pathways. Here, we examine the role of primary somatosensory cortex (S1) in touch-induced mechanical and heat analgesia. We found that, in mice, vibrotactile reafferent signals from self-generated whisking significantly reduce facial nociception, which is abolished by specifically blocking touch transmission from thalamus to the barrel cortex (S1B). Using a signal separation algorithm that can decompose calcium signals into sensory-evoked, whisking, or face-wiping responses, we found that the presence of whisking altered nociceptive signal processing in S1B neurons. Analysis of S1B population dynamics revealed that whisking pushes the transition of the neural state induced by noxious stimuli toward the outcome of non-nocifensive actions. Thus, S1B integrates facial tactile and noxious signals to enable touch-mediated analgesia.**

## INTRODUCTION

When a part of our body is hurt, we often instinctively rub, massage, or shake it. This phenomenon is referred to as touch-mediated analgesia, or pain relief by touch. It prompted the original development of the gate control theory (*1*). Subsequently, neurophysiological studies in anesthetized animals identified a class of wide dynamic range (WDR) neurons in the spinal cord, which receive both touch and pain inputs in the dorsal horn, as the likely substrate for the analgesia mediated by touch. The receptive field of WDR neurons has a center-surround concentric arrangement: The center is activated by tactile or nociceptive stimuli, whereas the surround is activated by noxious stimuli and inhibited by touch stimuli. Thus, vibrotactile stimuli applied around the noxious stimulus–sensitive center reduce WDR neuronal responses to the nociceptive inputs through inhibition (*2*–*4*). In humans, touch-mediated pain relief has been demonstrated for both body segments innervated by dorsal root ganglia (DRG) and orofacial regions innervated by trigeminal ganglion (TG) neurons (*5*). A quantitative study in humans, in which a painful laser stimulation was flanked by two touch stimuli at varying distances, showed that concurrent application of touch caused the subjects to rate the laser stimuli as less painful in a distance-dependent manner, consistent with the receptive field properties of spinal WDR neurons (*6*). The same study also found that although the "pinprick laser pain" sensation was reduced by concurrent touch stimuli, the latencies to detect the laser stimuli were not affected (i.e., noxious signals detected by Aδ fiber were relayed to the brain). This observation suggested that supraspinal mechanisms are involved in the "interpretation" of the laser stimuli as "less/non-painful" (*6*). Other human studies suggested a possible cortical involvement in this process (*7*–*9*). For example, tactile stimulus delivered 60 ms after the application of noxious electrical stimulus, whose signal has already reached the cortex by 60 ms, can still inhibit cortical responses to pain (*7*). However, if there is a cortical mechanism, which cortical areas would be involved remains unclear. Answering this question requires a reliable awake behaving animal model of touch-mediated analgesia.

While it is well known that vibrotactile information is mainly processed by the primary somatosensory cortex (S1), the exact role of S1 in nociception is still debated (*10*–*13*). Magnetoencephalographic, functional magnetic resonance imaging (fMRI), and electroencephalography (EEG) studies have reported inconsistent S1 activation during pain perception in human subjects, raising the question of whether S1 activation is required for nociception (*14*–*19*). On the other hand, studies in primates and rodents revealed that S1 or subregions within S1 were activated by noxious mechanical and heat stimuli (*10*, *20*–*23*). Recent studies further suggested that abnormal activation of S1 was linked to mechanical allodynia (*24*, *25*); however, layer 5 (L5) S1 corticospinal neurons were not involved in heat allodynia, although the authors did not investigate the role of S1 L2/3 neurons (*25*). Considering the inconsistent conclusions, it is important to examine whether S1 has the potential to integrate tactile and nociceptive (including noxious heat) information (especially in upper layers) to mediate touch-induced analgesia. Rodents use the whiskers as their main tactile sensors on the face. During environmental exploration, rodents move their whiskers back and forth at a high frequency, a process called whisking, to collect the sensory information in various contexts. Each whisker on the snout is individually represented in the S1 barrel cortex (S1B) (*26*, *27*). It has long been known that the S1B is dedicated to process whisker-derived tactile information such as the location, size, and texture of objects touched by the whiskers (*27*–*33*). By contrast, little is understood about whether and how S1B processes nociceptive information derived from the whisker pad skin. To develop a rodent orofacial model of touch-mediated analgesia, we hypothesized that whisking, as a form of vibrotactile inputs, might naturally suppress the nociception of acute noxious stimuli

[1]Department of Brain and Cognitive Sciences, McGovern Institute for Brain Research, Massachusetts Institute of Technology, Cambridge, MA 02139, USA. [2]Department of Neurobiology, Duke University, Durham, NC 27710, USA. [3]Department of Psychology and Neuroscience, University of North Carolina at Chapel Hill, Chapel Hill, NC 27599, USA. [4]Kirby Neurobiology Center, Boston Children's Hospital, Harvard Medical School, Boston, MA 02115, USA.
*Corresponding author. Email: fan_wang@mit.edu (F.W.); jinghaol@mit.edu (J.L.)
†These authors contributed equally to this work.

experienced by the face, and if so, this would provide a model to examine S1B′s role in touch, nociception, and their interactions. In this study, we tested our hypothesis and found that self-initiated whisking could suppress the mice′s nocifensive responses, and this effect was diminished when the transmission of whisking tactile signal from ventroposterior medial nucleus (VPM) in the thalamus to S1B was blocked. We further characterized the nociceptive representation in the L2/3 neurons of S1B and uncovered potential population activity patterns related to whisking-induced suppression of nociception.

## RESULTS

### Reafferent signals from self-generated whisking suppress facial nociception

The first question we asked was whether vibrotactile afferent signals of self-generated whisking would suppress orofacial nocifensive responses to noxious heat and mechanical stimuli in mice. We habituated head-fixed mice (C57BL/6J, $n = 13$, with 5 male and 8 female) on the running wheel and applied either radiant heat or noxious mechanical von Frey filament stimuli to the left whisker pad of the mice. Head fixation allowed consistent targeting of stimuli to the whisker pad (movie S1). Depending on the intensity of noxious stimuli they perceived, mice would either wipe their face, a nocifensive behavior, or not do so (Fig. 1A and movie S1). We operationally used this face-wiping behavior as a surrogate for nociceptive perception. We applied the stimuli when mice were either whisking in air (and running) or resting (no whisking) (Fig. 1A). We found that the number of face wiping in response to noxious heat or mechanical stimuli was significantly reduced when mice were whisking, compared to when mice were not whisking (Fig. 1B; $^{*}P < 0.025$, $^{**}P < 0.01$, or $^{***}P < 1 \times 10^{-4}$, when applicable). Similarly, the percentage of the trials in which mice wiped their face was also significantly reduced under conditions of self-generated whisking (fig. S1A).

To determine whether this reduction in nocifensive responses to noxious heat/mechanical stimuli was due to vibrotactile sensory signals generated by whisking (i.e., reafference) or due to an efferent signal (i.e., motor command for self-initiated whisking), we trimmed all the whiskers 1 day before behavior tests and repeated the same experiments. Even without whiskers, the whisking periods were apparent from facial muscle movements (movie S1). Nocifensive face wiping was not statistically different between whisking and non-whisking trials when whiskers were removed (Fig. 1C and fig. S1B; see fig. S2 for the response separated by sex). Similar results were obtained when only the whiskers on the same side as the stimulation were trimmed (C57BL/6J, $n = 7$, with 3 male and 4 female; fig. S1C). These results indicate that tactile reafferent signals derived from whisking in air, but not motor efference, play a critical role in suppressing facial nociception. The overall responses to heat and von Frey stimuli from mice with all whiskers removed differed from those in mice with only ipsilateral whiskers removed: Ipsilateral whisker removal produced a decrease in nociceptive responsiveness, especially in the non-whisk trials, which is the opposite effect from the bilateral whisker removal (compare fig. S1, B versus C, and Fig. 1C). It might be that ipsilateral and bilateral whisker removals engaged different plastic changes in the central circuits such that ipsilateral loss of whiskers rendered that side less sensitive, a topic beyond the scope of this study. Nonetheless, with intact whiskers, this behavioral paradigm provides a nice model to study the potential role of S1B (if any) in touch-mediated facial analgesia.

### S1B is activated by noxious stimuli

We first briefly summarize the pathways through which tactile and nociceptive signals from whiskers and whisker pad could both reach S1B (Fig. 2A) (*34*). Whiskers and whisker pad skin are innervated by the peripheral axons of TG sensory neurons whose central axons project to the principal sensory nucleus (PrV), which receives pure tactile (nonnoxious) sensory inputs, and to the trigeminal spinal nucleus (SpV), which receives both innocuous tactile and nociceptive inputs. Tactile signals are relayed from PrV to the contralateral dorsomedial region of the ventral posterior medial thalamus (VPMdm), and then to L4 and L5B of S1B. Nociceptive information are relayed from SpV to several thalamic nuclei, and to S1B, secondary somatosensory cortex (S2), and insular cortex (IC) (Fig. 2A) (*35*–*38*). While S2 and IC have long been recognized for their role in processing nociceptive information (temperature and pain), through the extensive intracortical connections between S2 and S1, and between IC and S1/S2 (*39*–*44*), noxious inputs to S2/IC can also reach S1B, positioning S1B as a site for touch/pain signal interaction.

To obtain initial evidence that noxious stimuli applied to the whisker pad can activate S1B (directly or indirectly), we performed wide-field calcium imaging of the cortical surface (see Materials and Methods; Fig. 2B, top; and fig. S3A) while applying either infrared laser (wavelength, 1450 nm) heat or noxious mechanical stimuli using the von Frey filaments to the whisker pad. Mice with cortical-wide GCaMP7f expressions ($n = 6$ in heat and $n = 5$ in von Frey experiment) were used for wide-field imaging. We first imaged cortical responses to piezo stimulation of individual whiskers to locate the borders of S1B (Fig. 2B, bottom, and fig. S3B). Subsequently, we applied laser heat (output power, 300 mW; duration, ~75 to 300 ms) or von Frey filament stimulations to the whisker pad (0.04 to 1 g) and recorded both the behavior and S1B calcium signals (movie S2). For noxious stimuli, operationally defined by stimuli that elicited wipes on ~50% trials, we observed clear S1B activations in response to both laser heat and mechanical stimulation (Fig. 2, C and E, and fig. S4, for the response to noxious von Frey stimuli in each mouse). We separated non-wiping trials, where activity was primarily stimulus driven, from wiping trials, where prolonged S1B activity likely reflected reafferent signals caused by wiping of the whisker pad area. We found that S1B responded significantly shortly after noxious mechanical and heat stimulation even when the animal did not wipe (Fig. 2, C to F; referenced to the baseline, von Frey 0.25 to 0.5 s: $P < 0.01$ for wiping trials and $P < 0.025$ for no-wiping trials; von Frey 0.5 to 1 s: $P < 0.01$ for wiping trials and $P = 0.94$ for no-wiping trials; heat 0.25 to 0.5 s: $P < 0.025$ for no-wiping trials and $P < 1 \times 10^{-4}$ for wiping trials; heat 0.5 to 1 s: $P < 1 \times 10^{-4}$ for wiping trials and $P = 0.19$ for no-wiping trials). Since S1B is well known for processing mechanical sensory information, we cannot conclude that S1B activation by noxious von Frey fibers reflected a specific nociceptive response from the wide-field imaging result (Fig. 2D; von Frey 0.25 to 0.5 s). However, noxious laser heat is a pure nociceptive stimulus. Thus, S1B can be activated by noxious heat experienced by whisker pad skin (Fig. 2F). Note that motor (M1) and premotor (M2) cortices were also activated, but their signals did not precede S1 (fig.

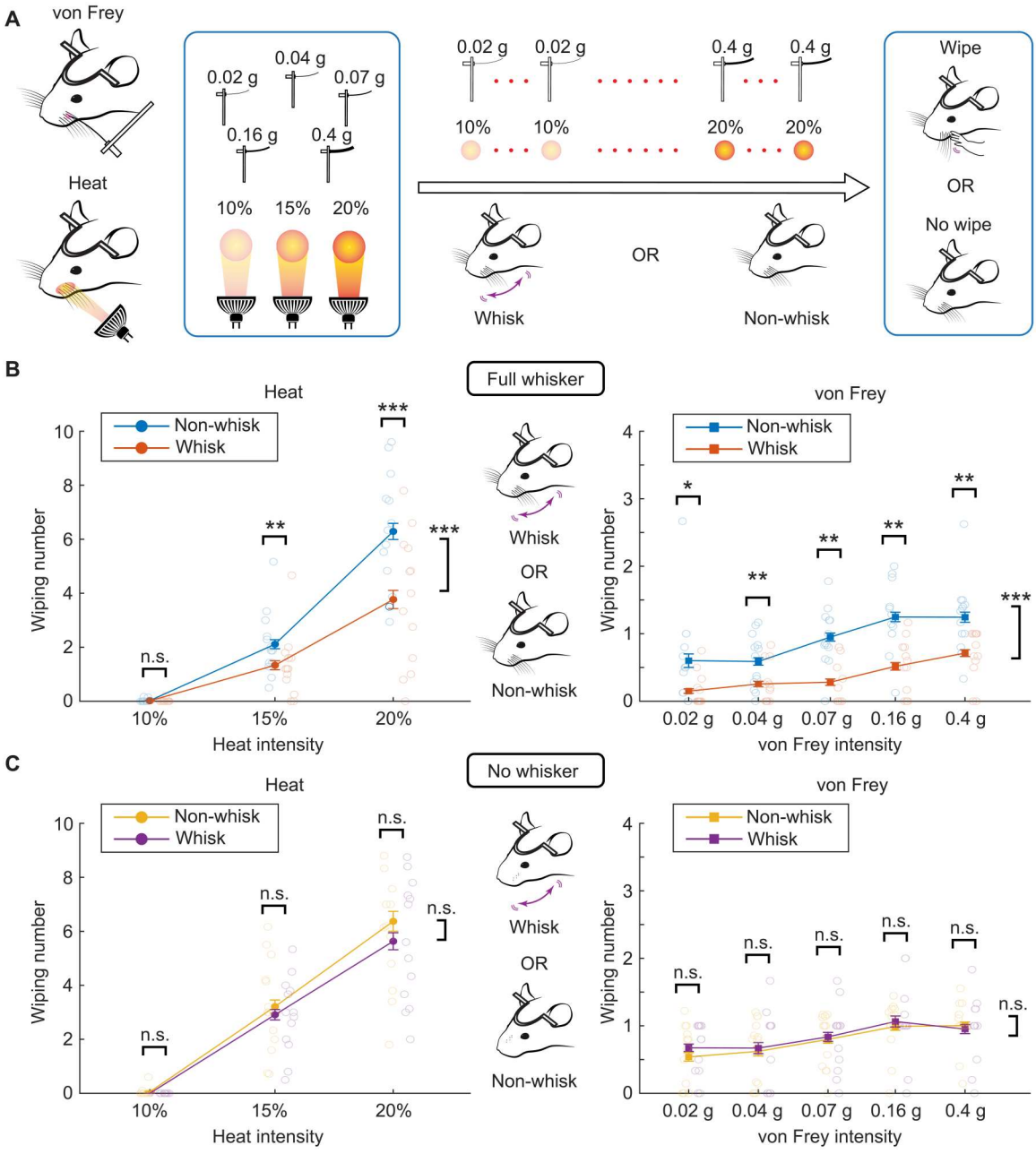


**Fig. 1. Reafferent signals from self-generated whisking suppressed facial nociception.** (**A**) Schematic of behavior experiments. Both heat and von Frey stimuli of various intensities were applied to the whisker pad of mice. Mice exhibited either wiping or no-wiping responses, and they were either whisking or resting (no-whisking) during the stimulus delivery. (**B**) Nocifensive responses to heat (left) or von Frey (right) stimuli measured by wiping numbers in mice with full whiskers (means and SEM). The trials were divided into whisking versus no-whisking conditions. (**C**) Similar to (B), except that stimuli were applied after all whiskers were trimmed (no-whisker) [$n$ = 13, 5 male and 8 female mice for (B) and (C)]. *$P$ < 0.025; **$P$ < 0.01; ***$P$ < 1 × $10^{-4}$; n.s., no significance. Repeated-measures analysis of variance (ANOVA) was used to test the main effect between full-whisker versus no-whisker conditions (indicated by a bracket on the side). Paired $t$ test was used to show the additional effect within the same stimulus intensity level.

S3C); hence, S1 activation was not a consequence of M1/M2 activation.

## Ntng1-Cre labels VPM neurons that mainly convey touch but not noxious signals to S1B

The existing anatomical pathways and our wide-field imaging results indicate that S1B could process both innocuous and noxious stimuli experienced by the whisker/whisker pad, and thereby potentially be involved in self-whisking–mediated facial analgesia. Since VPMdm specifically relays whisker-derived touch information to S1B, we first wanted to know whether blocking this "pure" tactile input pathway to S1B would abolish whisking reafference signal–induced suppression of nocifensive responses. We

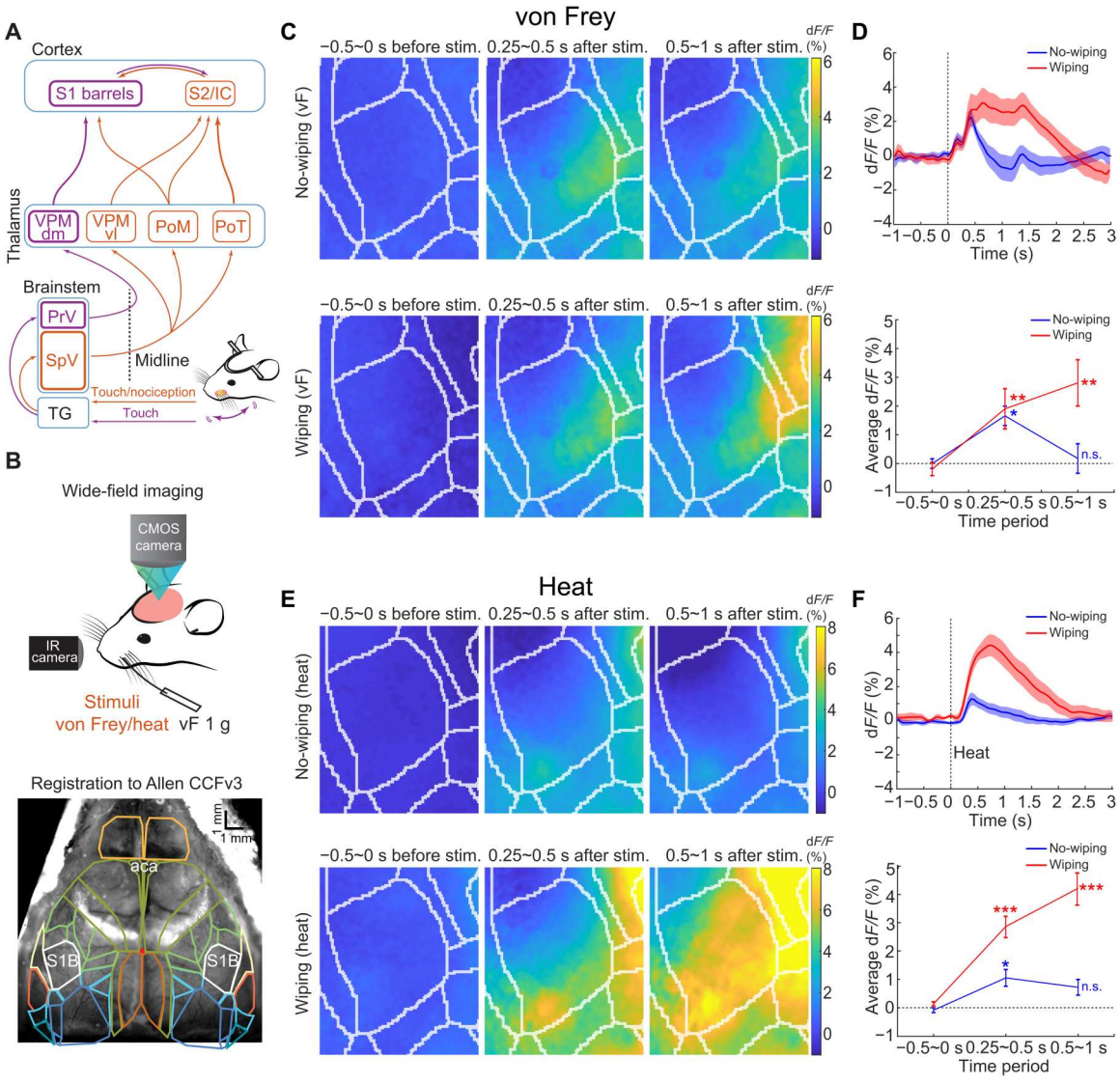


**Fig. 2. Wide-field calcium imaging showing that S1B is activated by noxious stimuli.** (**A**) Schematic diagrams showing the neuroanatomical pathways relaying touch and noxious signals experienced by the whisker pad from the periphery to different cortical regions. TG, trigeminal ganglion; SpV, trigeminal spinal nucleus; PrV, principal sensory nucleus; VPMdm, dorsomedial region of the ventral posterior medial thalamus; VPMvl, ventrolateral part of VPM; PoM, medial part of the posterior nucleus of the thalamus; PoT, the posterior triangular nucleus of the thalamus; IC, insular cortex. (**B**) Top: Setup for wide-field imaging of calcium activity. Bottom: The Allen atlas CCFv3 is scaled and rotated to fit the position of the imaged barrels. (**C**) Examples of d*F*/*F* maps of the barrel cortex imaged in a mouse stimulated with 1 g of von Frey fiber. Each map corresponds to the d*F*/*F* before stimulation (−0.5 to 0 s), when the stimulus first touches the face (0.25 to 0.5 s) and during the wiping period (0.5 to 1 s). Top: Average response across no-wiping trials ($n = 21$). Bottom: Average response across wiping trials ($n = 16$). (**D**) Top: Average response to noxious von Frey stimuli across mice ($n = 5$) with and without wipes (red, wipes; blue, no wipes; shaded area, ±SEM). Bottom: Average response during different time periods. (**E**) Examples of d*F*/*F* maps of the barrel cortex imaged in a mouse stimulated with 225-ms laser (1450 nm) pulse. Top: Average response across no-wiping trials ($n = 15$). Bottom: Average response across wiping trials ($n = 5$). (**F**) Top: Average response to noxious laser durations across mice ($n = 6$) with and without wipes. Bottom: Average response during different time periods. *$P < 0.025$; **$P < 0.01$; ***$P < 1 \times 10^{-4}$. Repeated-measures ANOVA was used.

recently generated an *Ntng1*-Cre knock-in mouse line in which Cre is expressed under the control of the endogenous *Ntng1* gene promoter (*45*). *Ntng1*, which encodes Netrin-G1 protein, has been shown to be expressed in the dorsal thalamus, and Netrin-G1 likely acts as a guidance molecule for thalamic axons projecting to S1 (*46*). To examine whether *Ntng1*-Cre–expressing VPM neurons ($VPM_{Ntng1}$) relay the "expected pure" tactile information to S1B, we first injected the AAV-Flex-GFP unilaterally into VPM of *Ntng1*-Cre mice and confirmed anatomically that the green fluorescent protein (GFP)–labeled $VPM_{Ntng1}$ neurons send dense axon projections mainly into the ipsilateral S1B to L4 and L5B (Fig. 3A, top). Next, to examine the in vivo activity of $VPM_{Ntng1}$ neurons, we injected AAV-Flex-GCaMP6m in the VPM of the *Ntng1*-Cre mice (Fig. 3A, bottom) and performed fiber photometry recording of their responses in different behavioral conditions.

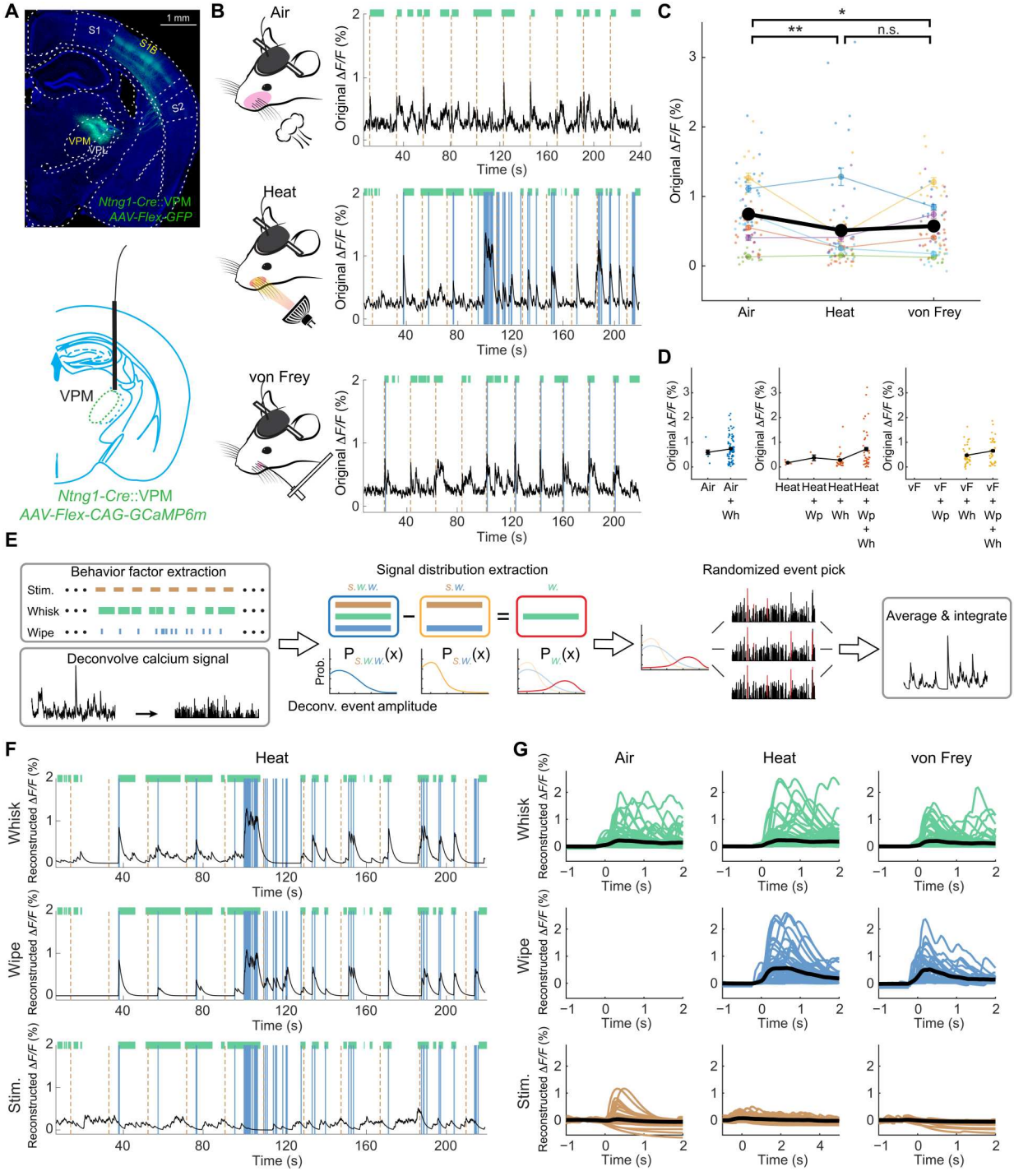


**Fig. 3. VPM$_{Ntng1}$ neurons mainly convey touch but not noxious signals to S1B.** (**A**) Top: Representative image of GFP-labeled VPM$_{Ntng1}$ neurons, and their axonal projections in the ipsilateral S1B L4 and L5B. Bottom: Schematic for the fiber photometry recording of the population activity from the VPM$_{Ntng1\text{-}GCaMP6m}$ neurons. (**B**) Representative VPM$_{Ntng1}$ population activity traces recorded by fiber photometry in different conditions. Air puff, heat, and von Frey stimuli were applied to the whisker pad of mice. Green bars, whisking periods. Orange dashed lines, stimulus onsets. Blue solid lines, wiping moments. (**C**) Maximum intensity of raw d$F/F_0$ from all trials for different stimulus types. Different colored dots represent trials from the same mice ($n = 6$ different mice). The colored line charts are the averages of maximum intensity of individual mice, while the black line chart is the grand average. (**D**) Maximum intensity of raw d$F/F_0$ from all trials separated further based on factors (stimulus, whisking, and wiping). (**E**) Schematics of the factor-related signal estimation algorithm with binary factor labeling. (**F**) Example traces of factor separated traces from one session of heat stimulus trials. (**G**) Separated signals epoched based on factors that were prefactor-corrected and aligned to the factor onset ($t = 0$) in different conditions, each line represents a trail from a mouse, and results from all mice are shown. The thick black line represents the grand average. *$P < 0.025$, **$P < 0.01$. Two-sample $t$ test was used to compare the maximum intensity of d$F/F_0$ from each trial for different stimulus types. Intensities of the noxious stimuli used: heat, 15% intensity; von Frey, 0.4 g.

Using the same head-fixed behavior setup described above, we applied either innocuous stimulus (air puff) or the two noxious stimuli (noxious heat 15% and von Frey mechanical stimuli 0.4 g) onto the whisker pad while recording the population calcium signal from the $VPM_{Ntng1}$ neurons (Fig. 3B; $n = 6$). The behavior was simultaneously filmed, and the periods of whisking and wiping events were manually tracked. We first compared the maximum intensity of $dF/F_0$ from each trial for different stimulus types (Fig. 3C; see Materials and Methods). On average, the $VPM_{Ntng1}$ neurons responded to air puff with stronger signal intensities than to heat or to von Frey stimuli, consistent with the primary role of VPM in signaling innocuous touch (Fig. 3C; $P < 0.01$ to heat; $P < 0.025$ to von Frey), and there was no statistical difference between responses to the two different noxious stimuli (Fig. 3C; $P = 0.485$). Because in each session, mice sometimes whisked when stimuli were applied or wiped their faces in response to the stimuli (note that wiping was never induced by air puff), we further separated the trials based on these two behavioral factors and then compared the maximum signal intensity. Whisking and wiping both increased the population activity when compared to the no-whisking or no-wiping conditions in response to the same stimulus type (Fig. 3D).

Because of the slow decay of GCaMP signals, the raw $dF/F_0$ population activity signals represent a mixture of external stimulus–elicited, as well as self-initiated whisking and wiping-generated signals. We therefore asked what the pure signals corresponding to different stimuli (air puff, heat, and von Frey) or to different behaviors (whisking or wiping) were for $VPM_{Ntng1}$ neurons. We first deconvolved the $dF/F_0$ signals into individual population calcium events using a constrained foopsi method (*47*) and then applied a signal separation algorithm that would extract the traces related only to one factor of interest (factor = stimulus, whisking, or wiping) (Fig. 3E; see Materials and Methods). Using heat trials as an example (Fig. 3F), this algorithm separated the raw $dF/F_0$ trace into pure whisk-, wipe-, and heat-related signals. In this case, the signals induced by whisking and wiping (both behaviors generate reafferent touch signals from whisker pad) were markedly higher than induced by heat. We performed this analysis for all trial types, and the pooled results are shown in Fig. 3G. As expected, the activity of $VPM_{Ntng1}$ neurons was dominated by tactile signals from whisking, wiping, and air puff and was minimally responsive to noxious heat or noxious mechanical stimuli (Fig. 3G). These results indicate that in awake behaving mice, $VPM_{Ntng1}$ neurons predominantly relay vibrotactile touch signals into the S1B.

### Inhibiting activity of S1B-projecting $VPM_{Ntng1}$ neurons diminished whisking-induced suppression of nocifensive responses

Next, we investigated whether blocking the main source of whisker-derived touch signals into S1B by inhibiting $VPM_{Ntng1}$ neurons would abolish the whisking-induced suppression of nocifensive responses. We injected AAV-Flex-$PSAML^{141F}$-GlyR-GFP into the VPM of *Ntng1*-Cre mice for transiently chemogenetic silencing $VPM_{Ntng1}$ neurons (Fig. 4A, left). PSEM308, the PSAM agonist, opens the $PSAML^{141F}$-GlyR chimeric ion channels to allow influx of chloride ions, thereby inhibiting the activity of the neurons expressing $PSAML^{141F}$-GlyR (*25*, *48*). Animals' responses to heat and von Frey stimuli (Fig. 4A, right) were measured at baseline (both pre- and post-PSEM sessions) and 20 min after PSEM308 administration (5 mg/kg, intraperitoneally; Tocris).

Again, we separated trials into whisking versus non-whisking ones. Analysis of trials with self-generated whisking revealed that during PSEM-mediated inhibition of $VPM_{Ntng1}$ neurons, both the percentage of trials with face wiping and the wiping numbers increased significantly in response to noxious heat and von Frey stimuli compared to those of no-drug conditions (pre- and post-drug baselines; Fig. 4B, $P < 0.01$, $1 \times 10^{-4}$, or $1 \times 10^{-6}$; Fig. 4C; $P < 0.01$ or $1 \times 10^{-6}$; $n = 8$). In other words, the whisking-mediated anti-nociception disappeared upon $VPM_{Ntng1}$ inhibition. As controls, PSEM treatment did not alter wiping responses during non-whisking periods, i.e., wiping behavior remained at the similar levels during the non-whisking trials in PSEM sessions compared to the baselines [Fig. 4, D and E; $P > 0.1$ using repeated-measures analysis of variance (ANOVA)]. Thus, inhibiting $VPM_{Ntng1}$ neurons did not alter normal nociception, consistent with our imaging results that these neurons do not convey nociceptive signals as they are pure tactile responders. Noxious information is relayed to the cortex by other thalamic and nonthalamic neurons. Together, these results indicate that whisking-mediated analgesia is diminished if the reafferent tactile signals are blocked from transmitting to S1B through the canonical VPM-S1 pathway. Since the main axonal target of $VPM_{Ntng1}$ neurons is S1B, these findings further underscore the essential role of S1B in integrating tactile and painful information to enable touch-mediated analgesia.

### In vivo miniscope imaging of S1B neuronal responses to noxious stimuli in behaving mice

Touch information transmitted by $VPM_{Ntng1}$ neurons to L4 S1B neurons is further relayed to L2/3 neurons. Nociceptive information could also arrive at upper layers of S1B either through the PoM (medial part of the posterior nucleus of the thalamus) pathway or via the intercortical connections with S2 and IC (Fig. 2A). Thus, L2/3 of S1B could be a node where tactile and noxious signals interact. To investigate how S1B might be involved in the touch-induced reduction in pain responses, we asked two main questions: First, how S1B differentiates innocuous versus noxious stimuli at the individual neuron level, and second, how S1B neural population represents whisking-induced suppression of nociception. To answer these questions, we decided to use in vivo imaging approaches to characterize S1B L2/3 activity. To ensure consistent imaging of the same S1B region across mice, we used intrinsic signal optical imaging to locate the activation area of the C2 whisker barrel in S1 cortex (fig. S5; see Materials and Methods) and then injected AAV-Syn-GCaMP6f into the L2/3 of the C2 barrel area in all animals ($n = 6$). We implanted the GRIN lens above the injection site to image calcium responses of individual S1B neurons using microendoscope/miniscope (Inscopix).

We performed in vivo imaging in head-fixed mice running on the wheel while applying innocuous (air puff) or noxious stimuli (heat, 15% intensity; von Frey, 0.4 g) to the whisker pad ($n = 6$; 6 sessions per mouse; see Materials and Methods). Calcium traces ($dF/F_0$) and the spatial footprints of the individual recorded regions of interest (ROIs) were extracted using MIN1PIPE (Fig. 5, A and B) (*49*). Pooling the trial average of all the neurons ($n = 764$ and 782 neurons, respectively, for heat and von Frey experiments from six mice) and then sorting neurons by their peak activity following the onset of either heat or von Frey stimulus delivery revealed that different neurons were activated at different time points in the 10-s window following stimulus onset, in both

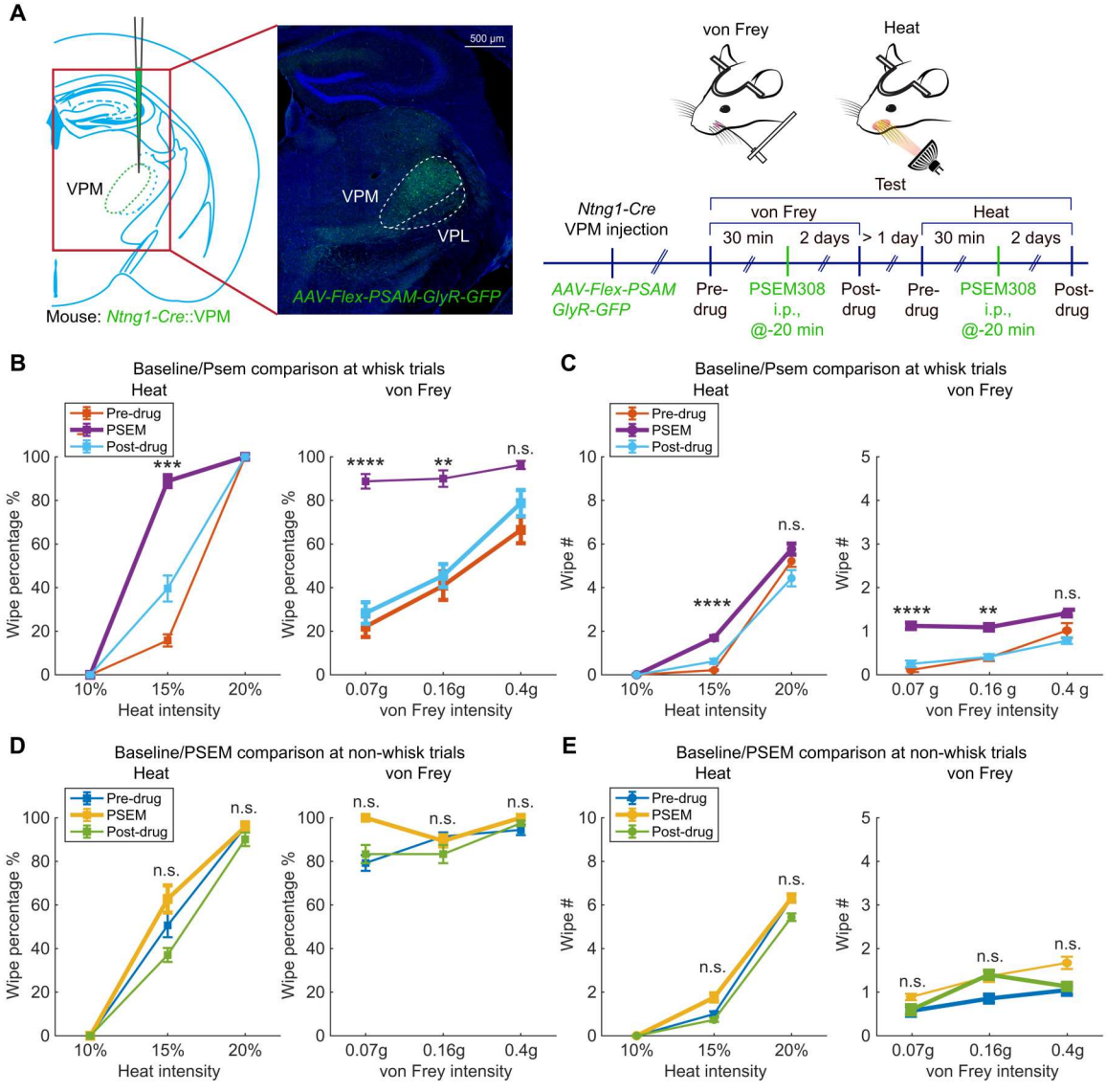


**Fig. 4. Inhibiting activity of VPM$_{Ntng1}$-S1B projecting neurons diminished whisking-induced suppression of nocifensive responses.** (**A**) Left: Schematic showing the manipulation strategy by injecting AAV-Flex-PSAM-GlyR-GFP into the VPM of *Ntng1*-Cre mice, and a representative image of the post hoc histology. Right: Timeline of von Frey and heat tests to assess the effect of the inhibition of VPM$_{Ntng1}$ neurons on the behavior. (**B** and **C**) Nocifensive behaviors in whisking trials of pre-drug, PSEM-administered, and post-drug sessions, measured by percentage of trials with wiping responses (B) or wiping numbers (C). (**D** and **E**) Nocifensive behaviors in no-whisking trials of pre-drug, PSEM-administered, and post-drug sessions, measured by percentage of wiping trials (D) or wiping numbers (E). $n = 8$ mice. $^{**}P < 0.01$, $^{***}P < 1 \times 10^{-4}$, $^{****}P < 1 \times 10^{-6}$. Repeated-measures ANOVA with post hoc Tukey's honestly significant difference was used.

whisking and non-whisking trial types (Fig. 5C). We also marked the time of wiping events (blue dots above the heat maps in Fig. 5C) to show that, in general, it took mice 3 to 4 s to wipe their face in response to heat (likely due to the slow heating up of the tissue and/or slower conduction velocity of heat-responsive c-fibers), whereas they wiped within 1 s upon von Frey stimulation (as noxious mechanical stimuli likely activate the fast conducting Aδ sensory fibers). In both heat and von Frey trials, there were subgroups of neurons with the rising phase of their calcium activity peaking before the onset of wiping behavior, suggesting that these subsets of neurons may signal the presence of noxious stimuli (Fig. 5C; see fig. S6 for alternative sorting strategies showing the nociceptive signal component and the dominant touch/wiping signal component). However, again, because of the intermingled nature of the signals likely reflecting a combination of external stimuli, whisking and wiping behaviors, it is difficult to draw conclusions based on the trial-averaged signals.

Therefore, we adapted the signal separation algorithm used above for the univariate fiber photometry data to the multivariate (i.e., multiple ROIs) miniscope calcium imaging data. We focused on isolating the specific sensory stimulus–related signals to examine whether S1B activity can distinguish different types of stimuli (innocuous air puff, noxious thermal, or noxious mechanical stimuli). For different stimuli, we used different time windows following the

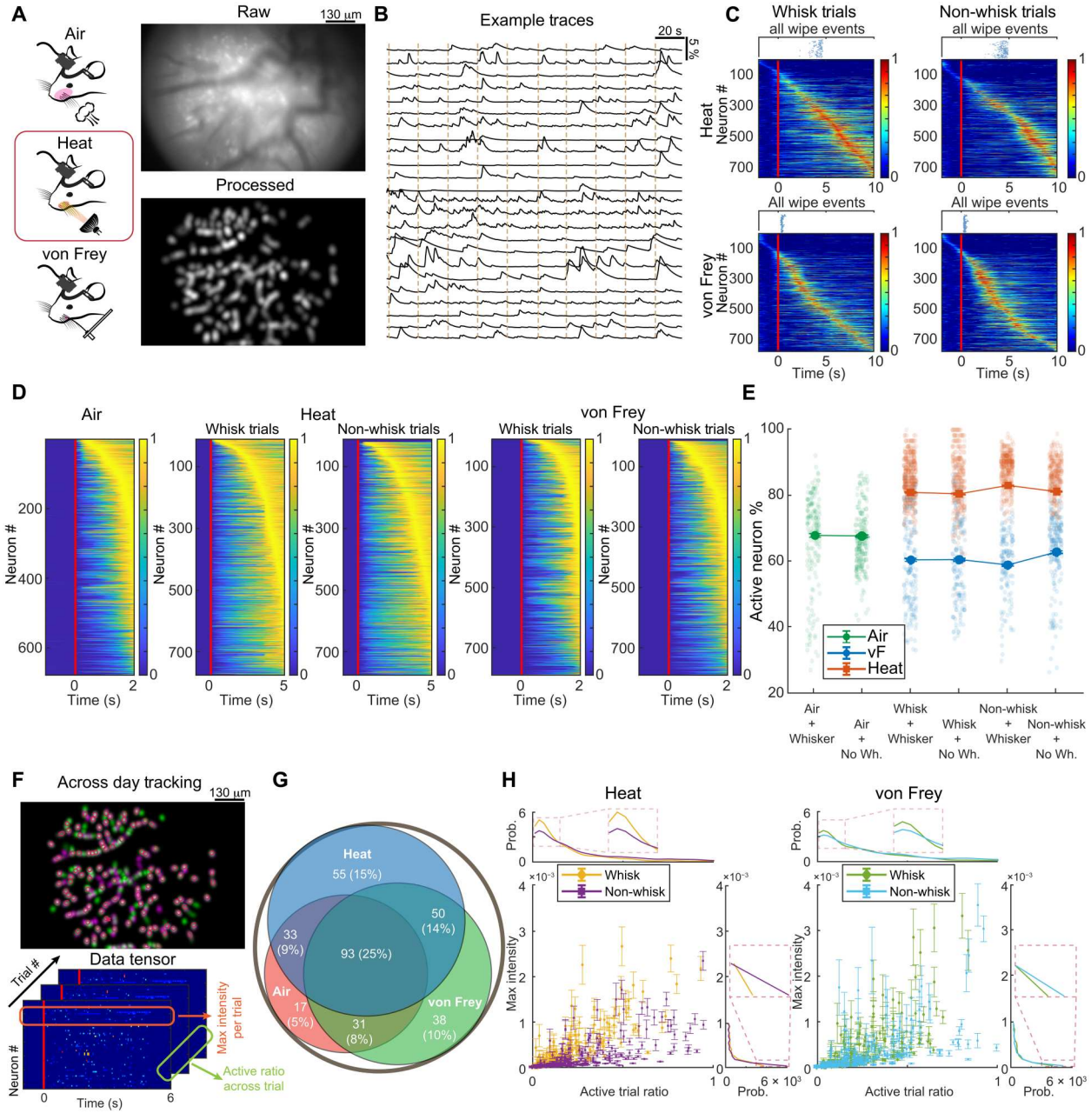


**Fig. 5. S1B L2/3 contains modality-specific and nonselective neurons, and whisking reduces their active trial ratios.** (**A**) Left: In vivo imaging while applying innocuous or noxious stimulus. Right: Raw field of view (top) and processed ROIs (bottom) of one representative imaging session. (**B**) Example traces of the extracted calcium fluorescence from the representative ROIs in an imaging session. Orange dashed lines indicating stimulus (heat) onsets. (**C**) Trial average of raw $dF/F_0$ for each neuron aligned to the stimulus onset (red lines). The traces were normalized. The first wiping events of all trials were also concatenated vertically and shown as blue dots on top of each heatmap. (**D**) Trial average of stimulus-specific signals (rescaled to [0, 1]) for each neuron aligned to the stimulus onset (red lines). (**E**) Percentage of active neurons per trial in response to different stimulus types (green, air puff; red, heat; blue, von Frey). The trials for noxious stimuli were further separated into whisking versus no-whisking and whisker versus no-whisker conditions. (**F**) Top: Example image of the same-neuron tracking for two different sessions of the same mouse. Red circles, tracked same neurons. Bottom: Demonstration of how to extract the two measures, maximum intensity per trial and active trial percentage, from the data tensor. (**G**) Venn diagram showing the distribution of stimulus-activated neurons (both absolute numbers and percentage of all the tracked neurons). (**H**) Scatterplots with means and SEM as a function of the maximum intensity per trial and active trial percentage, and the marginal distribution as a function of each variable. The trials were separated into whisking and no-whisking conditions. Intensities of noxious stimuli used: heat, 15% intensity; von Frey, 0.4 g.

onset of stimuli. Since we used an air blaster to deliver air puff, the stimulus lasted about 1 to 2 s. Considering the slower kinetics of GCaMP, we therefore analyzed imaging data up to 2 s following the onset of air puffs. For heat stimulations, the heating lamp was automatically turned off after 5 s, and mice showed wiping at around 3 to 4 s; thus, we analyzed signals up to 5 s. For von Frey, we manually applied von Frey for less than 1 s and then retracted the fiber, and wiping occurred at around 1 s (up to 2 s; wiping pushed away the von Frey filament, thereby terminating the mechanical stimulus sooner); thus, we analyzed calcium signals up to 2 s. The extracted stimulus-specific signals for imaged neurons were plotted as trial-averaged traces and sorted by their peak timing (Fig. 5D). These analyses revealed that S1B L2/3 neurons respond to both innocuous air puff to whiskers (as expected) and to noxious heat and punctate mechanical stimuli (that are generally perceived as noxious) applied to the whisker pad (with time course correlating with the duration of the stimuli) in both whisking and non-whisking trials (Fig. 5D). Note that the same method was applied to the VPM fiber photometry data, where very little heat or von Frey–related signals were found (Fig. 3G). Together, the results contrast the different roles of $VPM_{Ntng1}$ and S1B L2/3 neurons in touch-induced analgesia, with S1B being the potential site integrating touch/nociception information. To further validate that we extracted stimulus-specific signals, we applied our method to the baseline periods of imaging (where the data were not labeled with any of the factors of interest, namely, stimulus, whisking, or wiping), with the random labeling (i.e., assigned pseudo-stimulus, whisking, or wiping events). We then extracted the pseudo-factor–related signals and calculated the trial average for all neurons and did not find any obvious calcium events corresponding to pseudo-stimuli (fig. S7).

We further examined whether S1B population activity patterns showed modality-dependent (gentle touch, heat, and noxious mechanical stimulus) differences. For each trial, we used the stimulus-specific deconvolved calcium signals to calculate the adaptive threshold for each neuron and then extracted the number of active neurons (i.e., neurons with activity above the thresholds; defined by having at least one calcium event larger than 1 SD of the signal in each trial, with trial duration for air puff = 2 s, heat = 5 s, and von Frey = 2 s) (see Materials and Methods). We then pooled the data from the same types of trials and plotted the distribution of the active neuron ratios for each type (active neurons/all neurons per session; Fig. 5E). The results showed that, on average, ~67% of imaged S1B L2/3 neurons had calcium events in air puff trials, whereas ~80 or 60% of imaged neurons were active in noxious heat and von Frey (noxious or innocuous) trials, respectively (Fig. 5E). The stimulus-dependent active neuron ratios were similar in whisking/non-whisking and in full-whisker/no-whisker conditions. The differences in percentages of active neurons likely reflected the different stimulus duration (1 to 2 s for air puff, 4 to 5 s for heat, and 1 s for von Frey), as well as the size of the area affected by the stimulus (full whisker pad for air and heat versus a small locus on whisker pad for von Frey). The results suggest that the ratios of active neurons might be used to distinguish stimulus type.

To further determine whether S1B L2/3 contains neurons that are specifically tuned to different stimulus modalities, we tracked neurons imaged in each mouse across different sessions, using the modified CellReg algorithm (*50*), and examined their responses to different stimuli (Fig. 5F). Of all the neurons, we successfully tracked 365 neurons. Using the same adaptive thresholding approach (see Materials and Methods), we determined whether each tracked neuron was activated in response to air puff, heat, or von Frey (Fig. 5G). The Venn diagram shows that although a subgroup of neurons ($n$ = 93) nonspecifically responded to all three types of stimuli, there were comparable subgroups of neurons that were either active in two types of stimuli or only specifically activated by a single type of stimulus (Fig. 5G). Thus, in principle, the modality-specific single neurons, together with the overall ratios of active neurons mentioned above, could enable S1B to discriminate gentle touch versus noxious heat versus punctate mechanical stimuli (which is largely noxious in the absence of whisking).

### Analyzing the effect of whisking on activity of individual S1B L2/3 neurons in response to noxious stimuli

While the analyses described above provide evidence for the involvement of S1B in processing and potentially discriminating gentle versus noxious touch versus heat, it did not reveal how whisking-derived reafference touch signals might alter how S1B neurons process noxious information. To begin to understand this question, in the same-cell tracking process, we also extracted the maximum intensity per neuron per trial and the percentage of active trials for each tracked neuron (active trials/all trials per session) using the deconvolved stimulus-specific calcium signals (active trials defined by having maximum intensity of deconvolved events above 1 SD of all trials′ maximum intensity; see Materials and Methods for details; Fig. 5F). We further separated trial types into whisking versus non-whisking ones, as shown in Fig. 5H, main panels. We also calculated the probability density function for these two measures (Fig. 5H, top and right).

We found that whisking slightly decreased the proportion of neurons with lowest maximum intensity [see probability density on the right side of the heat and von Frey plots in Fig. 5H; Kolmogorov-Smirnov test (KS test) with $P < 0.001$ for heat but $P > 0.01$ for von Frey using trial-averaged data; however, if using all trial data rather than trial-averaged data, the KS test showed significance with $P < 0.001$ for both conditions]. In other words, whisking increased the baseline activity of those inactive/silent neurons. This is likely due to the propagation of whisking signals in S1B that increased basal activity of L2/3 neurons. However, the probability density at high maximum intensity was almost unaltered by whisking. On the other hand, our analyses also revealed that most S1B L2/3 neurons were only activated (compared to their own baseline activity) in low percentages of trials and had low activity levels, consistent with the sparse coding mode of L2/3 neurons observed previously (*51*). Whisking further reduced S1B neurons′ overall responsiveness to heat and von Frey by increasing the proportions of neurons with low percentage of active trials (see probability density in top panels of Fig. 5H; KS test showing $P < 0.01$ for heat but $P > 0.01$ for von Frey using trial-averaged data; however, if using all trial data rather than trial-averaged data, the KS test showed significance with $P < 0.001$ for both conditions). In other words, whisking makes S1B L2/3 neurons as a population less likely to respond to subsequent noxious stimuli. This result is consistent with previous studies revealing that whisker-derived inputs to L4 can mediate feedforward inhibition of L2/3 neurons (*29*, *35*). While previous work only examined tactile processing, our results suggest that this whisking-derived feedforward inhibitory

mechanism also contributes to the suppression of S1B nociceptive responses.

### Tensor component analysis revealed the differences in S1B population activity between trials with or without nocifensive responses

To further investigate what aspects of S1B population activity patterns (rather than highest intensity) correlate with nociception, we performed tensor component analysis (TCA) (*52*) to analyze the raw $dF/F_0$ data in heat and von Frey trials. TCA, compared to the traditional trial-averaged principal components analysis (PCA), enables dimension reduction capturing single-trial dynamics. Briefly, using the method described in (*52*), as shown in Fig. 6A, we applied TCA to decompose the data tensors (a collection of matrices) obtained from raw fluorescence signals into factors corresponding to neuronal (i.e., assemblies of neurons), temporal (i.e., neural dynamics shared by all trials), and trial (i.e., trial-to-trial scale changes of the same temporal factor) components (Fig. 6A and fig. S8; see Materials and Methods). Because we used wiping behavior as the surrogate for pain perception, we mainly wanted to identify the differences in neuronal patterns between wipe and no-wipe conditions in both heat and von Frey trials. We extracted multiple tensor components (TCs) per mouse for each type of trial, whose trial factors had the highest similarity score with the actual behavior readouts (wipe versus no wipe, and further separated into whisking versus no-whisking trials) (Fig. 6B).

For the extracted TCs from all mice, we placed them into 1-s bins (the whole duration of a trial is 5 s) and pooled (summed up) the TCs in the same time bin into "clustered components" (illustrated in Fig. 6A). We then compared the amplitudes of the clustered components in the time window right before the wiping behavior (the surrogate for nociception), i.e., [2 to 3 s] for heat and [0 to 1 s] for von Frey trials. This analysis showed that in conditions where there was no nocifensive wiping, regardless of whether whiskers were present or all-removed and whether mice were whisking or not whisking, the clustered TCs in the pre-wiping window had smaller amplitude than the ones exhibiting wiping behavior (Fig. 6B; note that in heat experiments, the no-wiping conditions had zero amplitude, thus not observable on the figure). In other words, S1B L2/3 population activity differed between trials with or without nocifensive behaviors in the pre-action window, which could be considered as the window when noxious information might be perceived. Larger clustered components (i.e., total behavior-specific neural dynamics) correlated with subsequent nocifensive actions, consistent with the idea of S1B as a sensorimotor cortex (see Discussion). On the other hand, we attempted to compare wiping trials with or without whisking to uncover the potential role of whisking in suppressing wiping. However, because of the dominance of wiping signals, we did not detect any specific component that could explain how might whisking work in non-wiping trials compared to wiping trials.

### Whisking suppresses nocifensive behavior through moving S1B neuronal population dynamics toward the nonpainful states on the intrinsic manifold

Since the TCA analysis did not uncover the exact effect of whisking on nociception, we turned to examine the state space formed by the population activity of S1B neurons for each session (i.e., imaged neurons, their activity recorded over time throughout the entire session) to answer this question. All states for a given session in the high-dimensional state space (number of dimensions = number of neurons) are assumed to belong to a (continuous) manifold, which has lower intrinsic dimensions embedded in that state space (fig. S9). To find/approximate the presumed intrinsic manifold, we applied a manifold learning algorithm (*53*, *54*) and then calculated the metric that geometrically defines the manifold to reconstruct the Riemannian manifold (Fig. 6C; see Materials and Methods) (*55*, *56*). Examples of the learned manifolds for two different sessions projected onto three-dimensional space are shown in Fig. 6D, where each dot is the projected state from the manifold to the space spanned by the first three dimensions. Using persistent homology analysis (*57*), we found that all learned manifolds were continuous ($\beta 0$) with no general holes ($\beta 1$; fig. S10), suggesting that these manifolds all have the same trivial topological property (single connected component).

Having computed the lower-dimensional manifolds, we asked whether the subspaces for different behavioral configurations (i.e., different combinations of whisking/no-whisking and wiping/no-wiping) corresponded to orthogonal dimensions or largely shared the same subspace (Fig. 6E). In other words, we looked for extent of commonality between population dynamics for different behaviors. To answer this question, we further reduced the dimensions of each subspace using PCA and kept the first $N$ components whose cumulative explained variance exceeded 99%. The average number of dimensions stayed relatively constant across all configuration subspaces (Fig. 6F; see Materials and Methods). Analysis of the shared dimensions across different subspaces within the same session and mouse showed that most of the dimensions between any two pairs of behavioral configurations were orthogonal in both heat and von Frey trials (Fig. 6G). A general summary of the shared dimensions across all degrees of behavioral configurations further confirmed this observation (Fig. 6H). That subspaces occupied by different types of behaviors are mostly orthogonal suggests that whisking alters S1B population neural dynamics in response to heat or von Frey differently than non-whisking conditions, thereby resulting in different nociception and responses (wiping versus no wiping). It is also possible that in trials with no whisking, other factors (e.g., animal's attention and internal state) may alter S1B dynamics to cause lack of nociception (and thus no wiping).

To better define the role of whisking, we measured the length of the trajectory traveled by the activity of S1B neurons on the manifold for each trial (which starts with stimulus onset and ends roughly 5 or 1 s after applying heat or von Frey, respectively). We applied a shortest path algorithm on every two neighboring states of a trial on the learned Riemannian manifolds and summed up the total geodesic distances (Fig. 6I). Since the manifolds do not necessarily scale in geometrically equivalent manner, we normalized the calculated trial trajectory length to the ones with both whisking and wiping (Fig. 6J). In general, the trials with wiping (indicative of nociceptive perception) had shorter trajectories than the trials without wiping in response to both heat and von Frey (Fig. 6J). This is likely due to the fact that nocifensive face wiping upon sensing noxious stimuli is a stereotypical response, with low-energy barrier between the state of sensation (nociceptive stimuli sensed) and the state of action (wiping). Notably, among the wiping trials (in which pain is presumably sensed), the trajectory in non-whisking conditions was the shortest, shorter (below the red dashed line in

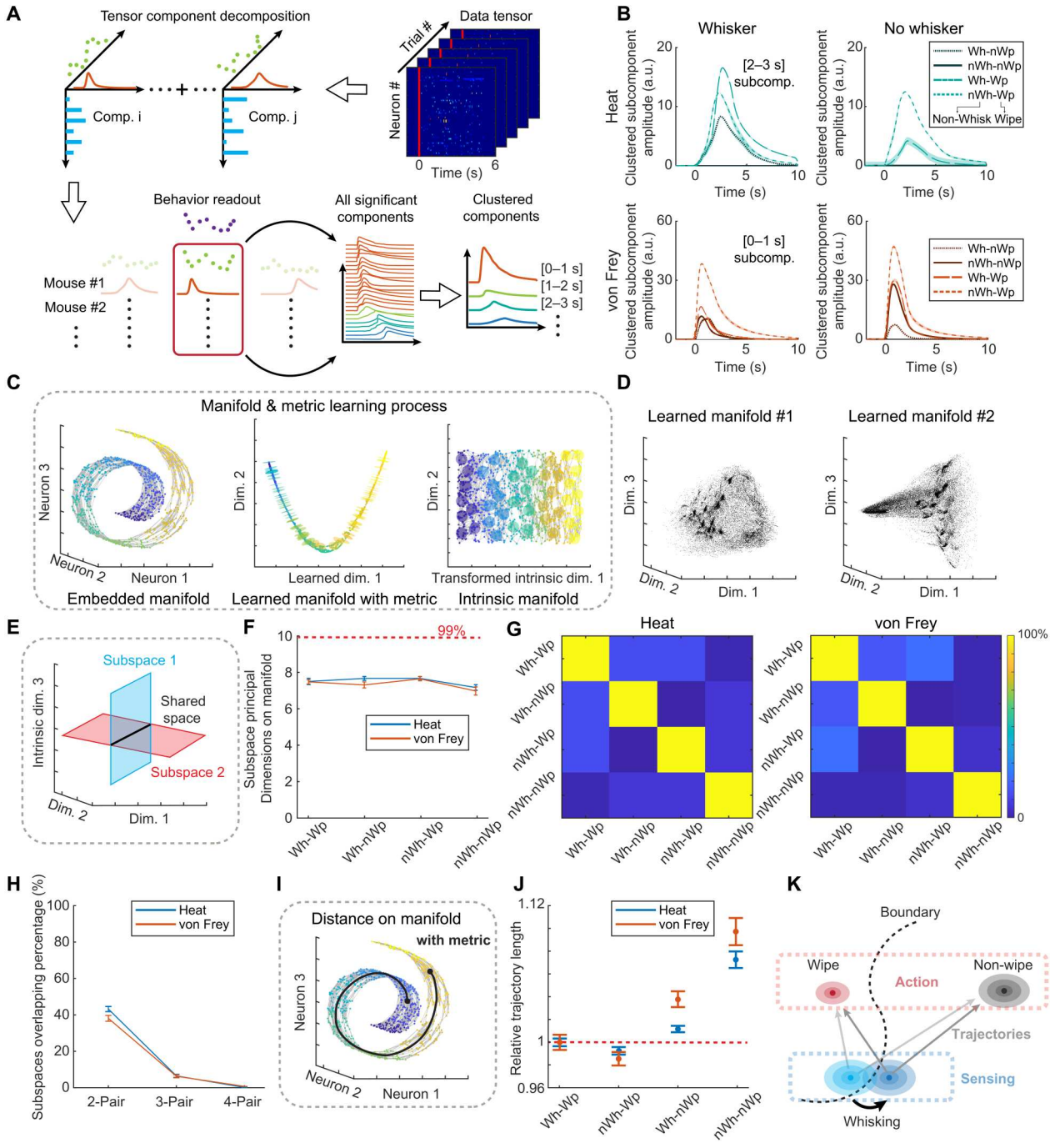


**Fig. 6. Whisking moves the S1B population dynamics toward the no-nociception–no-action states on the intrinsic manifold.** (**A**) Schematic of the processing pipeline using TCA. (**B**) Amplitudes of clustered components for different behavioral combinations (whisking/no whisking and wiping/no-wiping) in response to heat or von Frey stimulation in full-whisker and no-whisker conditions. The no-wiping conditions in the heat experiments did not have TCs in the time bin (zero amplitude). (**C**) Steps to learn the intrinsic manifold and to estimate the point-wise metric, shown with a toy model (swiss roll). (**D**) Examples of learned manifolds (without correction with metric) from two sessions. The states (individual black dots) were projected onto the first three dimensions of the intrinsic dimensions learned with Laplacian Eigenmaps (LEM). (**E**) Schematics for how we define shared spaces by the two subspaces on the manifold formed by the two different behavioral configurations. (**F**) Average number of dimensions of S1B neural activity in each behavioral configuration from PCA. The first *n* principal components (dimensions) whose cumulative variance of neural activity explained exceeded 99% were preserved. Red dotted line: Dimension that has 99% of variance in an isotropic space. (**G**) Numbers of dimension of the shared space between any pair of subspaces formed by different behavioral configurations, shown in the form of heatmap matrix. (**H**) General summary of the dimensions of the shared space across any combination of the subspaces formed by different behavioral configurations. (**I**) Schematic for how trajectory length is calculated along the intrinsic manifold. (**J**) Summary of the trajectory lengths (means with SEM, averaged across trials) along the manifold, grouped by the behavioral configurations and normalized to the average trajectory length of the whisking-wiping configuration. (**K**) Schematic summary S1B population dynamics underlying whisking-induced analgesia. Intensities of noxious stimuli used: heat, 15% intensity; von Frey, 0.4 g. a.u., arbitrary units.

Fig. 6J) than that of wiping trials with whisking. This finding suggests that when S1B neural activity likely signals the detection of noxious stimuli, whisking pulls the trajectory away from nociception, thereby lengthening the distance of the neuronal state to the action outcome of wiping. By contrast, in the non-wiping trials (in which the noxious stimuli failed to be sensed), the presence of whisking resulted in a shorter trajectory than that of no-whisking trials. This result suggests that whisking facilitates (i.e., shortens) the trajectory toward the action outcome of non-wiping (Fig. 6K, schematic). The non-whisking–non-wiping trials likely reflect an effect of internal state on nociception, and they have longest trajectory. Together, our results, along with other studies on the role of S1 in decision making (*58*, *59*), support the role S1B L2/3 neurons' population dynamics in integrating peripheral-derived diverse somatosensory stimuli and steering the brain states toward different actions. S1B is an important node in mediating the phenomenon of pain suppression by vibrotactile touch. This is achieved by a mechanism in which self-generated whisking inputs move the initial population dynamics in response to noxious inputs toward the states signaling innocuous touch and thus reducing the need for nocifensive actions.

## DISCUSSION

In this study, we developed a mouse behavioral model of vibrotactile touch–mediated suppression of nociception. We showed that reafferent signals from self-generated whisking reduce nocifensive wiping responses to noxious heat and mechanical stimuli applied to the face. This effect requires the transmission of innocuous tactile signals through the VPM to S1B pathway, pointing to the involvement of S1B in whisking-induced face analgesia. In vivo calcium imaging of S1B L2/3 neurons during this behavioral paradigm revealed the existence of modality-specific and modality-general S1B neurons, and that whisking moderately reduced the overall responsiveness of individual S1B neurons to noxious mechanical and heat stimuli. TCA further uncovered consistent differences in S1B population activity before the different action outcomes (wiping or no-wiping) in response to noxious stimuli, supporting the role of S1B in sensation and sensation-guided action. Last, by analyzing the intrinsic manifold equipped with metric, we found that S1B activity in wiping (nociception) versus no-wiping (lack of nociception) trials occupies different subspace on the manifold of S1B state space, and importantly, preexisting whisking pulls the S1B dynamics away from the nociception-to-wiping trajectory while facilitating the state transitions along the no-nociception–no-wiping trajectory.

While pain relief by touch is a common human experience, a simple and robust animal behavior model has not been previously established. Instead, electrophysiological studies had largely focused on spinal mechanisms using anesthetized animals. Most animal behavior studies have focused on the opposite phenomenon: pain-induced tactile allodynia (i.e. under painful conditions, animals show hypersensitivity to gentle touch), due to the ease of applying external tactile stimuli to painful areas. While animals clearly use behaviors involving self-generated touch, such as licking and wiping of a hurt body part to relieve pain, these behaviors contain mixed components of pain, touch, and movements and lack a means to measure/report the changes in the perceived pain induced by licking/wiping. Without an easy and reproducible awake behaving animal model, it is difficult to examine whether supraspinal centers (and where) are involved in touch-mediated analgesia. Here, taking advantage of the natural whisking behavior in mice, which is readily exhibited in head-fixed preparation, we showed that the whisking-derived vibrotactile reafferent signals can significantly reduce nociception to noxious heat or mechanical stimuli applied to the face, thereby establishing a simple yet robust behavioral paradigm for studying touch-induced analgesia. Note that we used face wiping as a surrogate for pain perception by the mouse. Unlike the simple head withdrawing away from the stimuli (in head-free mice), this goal-directed action of moving the ipsilateral forelimb and forepaw toward the face and wiping the stimulated region is not a simple low-level reflex. This behavior likely requires localizing the stimulus to the face, perceiving the stimulus as noxious, and generating a motor action to relieve the transient pain, making it a reasonable surrogate for pain perception.

Using this natural behavior paradigm, we uncovered the role of S1B barrel cortex in whisking-mediated face analgesia, since blocking the tactile-specific thalamocortical pathway from $VPM_{Ntng1}$ to S1B largely abolished the analgesic effect of whisking, but had no effect on nociceptive responses in non-whisking conditions. A long history of studies on the rodent S1B has highlighted its role as the primary cortical region that processes whisker-derived tactile information (*27*, *28*). The well-known functions of S1B include object localization and texture perception, as well as integration touch with locomotion. However, whether and how S1B is involved in processing painful stimuli experienced by the face (whisker skin) have been poorly studied, especially in awake behaving rodents. Part of the difficulties of studying pain processing in S1B in awake animals is that noxious stimuli elicit immediate nocifensive behaviors, making it hard to separate stimulus-related versus behavior/movement-related signals. The slower decay of the calcium indicator makes separating signals even more of an issue. Recent brain-wide electrophysiological recordings or calcium imaging studies all revealed that behavior/action signals are prominent and widely spread throughout the brain (*60*–*62*). Here, we developed a signal estimation algorithm that enables extraction of specific neural signals corresponding to stimulus or behavior from both fiber photometry and calcium imaging data. Using this algorithm, we confirmed that $VPM_{Ntng1}$ neurons relay primarily innocuous tactile stimuli but are minimally responsive to nociceptive stimuli. Furthermore, we found that S1B L2/3 neurons can be activated by innocuous touch, heat, and noxious mechanical stimuli. Our wide-field imaging also showed S1B activation by noxious von Frey fibers and laser heat, although the responses to heat trials were smaller compared to those in von Frey trials (likely due to the focused laser beam heating only a small area and the von Frey stimulus also evoking activity in non-nociceptive mechanosensitive neurons; therefore, for fiber photometry and miniscope imaging studies, we used heating lamp to heat a larger area). S1 may not be the "entry node" for heat signals in cortex; rather, S2/IC may be where heat signals first arrive at cortex (*15*, *17*, *63*), and the extensive cortical-cortical connections would still allow heat signals to reach S1. We further found that while there are many S1B neurons that nonspecifically respond to all types of sensory stimuli, a subset of S1B L2/3 neurons are only activated in response to a single modality, consistent with the previous evidence in lightly anesthetized primates and rodents (*10*, *64*). The signal separation algorithm can

be applied to other behaviors with mixed sensory and motor components.

From our single neuron analyses, we found that whisking had a moderate effect on the overall activeness of S1B L2/3 neurons, i.e., whisking further decreases the percentages of active trials of individual neurons in response to noxious stimuli. This finding is consistent with previous studies showing that whisking inputs onto L4 of S1B mediates feedforward inhibition of L2/3 neurons (*29*, *35*), although previous studies focused solely on tactile stimuli. This inhibition could partially contribute to the whisking-mediated analgesia. On the other hand, whisking had no obvious effect on the highest signal intensities of active neurons in response to noxious stimuli (it only slightly increased the lowest signal intensities). We observed strong S1B neuron responses to innocuous air puff to whisker and during wiping (as expected). These results suggest that the maximum high intensity of S1B neurons is unlikely a good indicator of pain versus no pain sensation. This idea is completely in line with human EEG and fMRI studies. Human studies showed that the correlation between the magnitude of brain activity in any of the pain-processing cortical areas (S1, S2, IC, and anterior cingulate cortex) and the subjective pain is poor and can even be dissociated in opposite directions, i.e., there could be prominent activity when no pain is experienced, or there could be small amplitude activity when intense pain is experienced (*13*, *65*).

Thus, we examined the population-level neural dynamics of S1B to extract patterns that are correlated with pain versus no pain responses, and the role of whisking. Using TCA, which is essentially fitting a gain-modulated linear network to the observed S1B activity, we found that larger TCs before the expression of nocifensive responses are consistently associated with the subsequent wiping behaviors. While we use wiping as a surrogate for pain being perceived, our finding is consistent with previous studies uncovering choice/decision-related signals in S1B using other behavioral paradigms (*32*, *59*). In this regard, S1B can be considered as a region for sensorimotor transformation. The topographic organization of S1B can provide precise spatial information needed to generate a motor plan for an effector (a limb) to target the location (whisker pad). In this framework, the role of whisking could be altering the sensorimotor transformation process, thereby leading to a different action (i.e., no wiping in our case). By projecting the high-dimensional S1B neural activity in each session onto a lower-dimensional intrinsic manifold (using manifold learning methods with metric recovery), we were able to calculate the trajectories of S1B population activity in different trials. Despite the fact that the intrinsic manifolds we found from the S1B imaging data might vary across days and across animals, likely due to the variations in experimental conditions (e.g., changes in focus plane, differences in GCaMP expression levels, and low resolutions of miniscope imaging), we nevertheless found that whisking consistently moved the trajectory further away from wiping while shortening the trajectory to the no-wiping action outcome in all cases. Future experiments with larger dataset and higher spatial and temporal resolution imaging may reveal a more salient manifold for S1B neural activity.

Note that it has been increasingly recognized that the repetitive behaviors observed in autistic patients (often referred to as "stimming") have a soothing effect on these patients, but the neural mechanisms remain vague. Stimming generates vibrotactile reafferent inputs. With numerous mouse models of autism available, it will be interesting to examine how whisking alters nociceptive processing in both subcortical and cortical levels in these autism models, and perhaps aids future development of devices that can mimic the calming effect of repetitive stimming. Last, pain is a complex sensory and emotional experience that can be altered by higher-order processing and is subject to extensive descending controls from cortical and subcortical regions. Our study advances the studies on supraspinal modulations of pain perceptions (*12*, *25*, *66*, *67*).

## MATERIALS AND METHODS

### Animal statement

All experiments were conducted according to protocols approved by the Duke University and Massachusetts Institute of Technology (MIT) Institutional Animal Care and Use Committee.

### Animals

Adult (8 to 12 weeks) C57BL/6J, *Ntng1*-Cre (*45*), or Ai162; slc17a7-Cre mice (JAX no. 031562; JAX no. 023527) were used for the experiments. Animals were housed in the vivarium with a 12-hour light/dark cycle and were given food and water ad libitum. Mice were singly housed after GRIN lens implantation.

### Viruses and reagents

AAV2/8-CAG-Flex-GFP (Addgene no. 59331), AAV2/1-CAG-Flex-GCaMP6m (Addgene no. 100839), and AAV2/8-Flex-PSAML$^{141F}$-Y115F-GlyR-IRES-GFP (Addgene no. 119741) viruses were used for VPM studies. AAV2/1-Synapsin-GCaMP6f (Addgene no. 100837) or AAV PHP.eB.syn.jGCaMP7f (Addgene no. 104488) was used for S1B imaging studies.

PSEM308 hydrochloride was purchased from Tocris (catalog no. 6425) (*68*) and administered (5 mg/kg, intraperitoneally) at 20 min before the behavior test.

### Stereotactic surgical procedures

Mice were anesthetized with isoflurane (3% induction and 1% maintenance) and placed on a digital stereotaxic frame (David Kopf Instruments) with a heating pad. An incision was made in the scalp, and tissue was gently removed to expose the skull. The skull surface was treated by dentin activator (Parkell) before proceeding to the following procedures.

For viruses expressed in the VPM, small craniotomies were made on the brain surface at the appropriate coordinates [right VPM: +1.95 mm anterior-posterior (AP), +1.85 mm medial-lateral (ML), and −3.20 mm dorsal-ventral (DV)], and viruses (0.3 to 0.6 μl) were infused at a rate of 50 nl/min using a glass micropipette connected to a Hamilton syringe by tubing filled with mineral oil and left for 10 min after infusion to allow for diffusion.

For fiber photometry recording in the VPM, fiber optic cannula (200-μm core, 0.39 numerical aperture; RWD) was implanted 200 μm above the VPM after virus injection and secured to the skull using super glue (LOCTITE).

For behavior tested on the treadmill, horseshoe-shaped headposts were placed on the skull, Metabond (Parkell) was applied to secure the headpost to the skull, and dental cement darkened with carbon powder was used to cover the skull over the top surface.

For intrinsic imaging in the right S1B, a small ink marker for the target (right S1B, +1.5 mm AP and +3.5 mm ML) was made on the

skull. Headpost was then secured to the skull, and dental cement darkened with carbon powder was used to cover the skull except for the 4- to 9-$mm^2$ window above the barrel cortex. After the dental cement dried, the barrel cortex window was cleaned and filled with saline, which can visualize the surface blood vessels. Ultraviolet (UV)–curable adhesive was applied quickly after removing saline with a cotton swab to visualize blood vessels for intrinsic imaging. Subsequently, mice were kept on the heating pad for recovery and returned to the homecage for further intrinsic imaging.

For the GRIN lens implantation in the S1B, after aligned location of C2 barrel with cortical vasculature based on the intrinsic imaging data, mice were anesthetized with isoflurane and placed on stereotaxic frame, UV optical adhesive was carefully removed, and a craniotomy (1.5 to 2 mm × 1.5 to 2 mm) was made on the brain surface, avoiding damage to the cortex. The craniotomies were shifted medially about ~20° on a horizontal plane for the virus injection. Viruses were (0.6 μl total) infused at a rate of 10 nl/min into three locations (−0.25 mm DV) to evenly label the intrinsic signal location. Thirty minutes after virus injection, the GRIN lens (4 mm × 1 mm, Inscopix) were tightly attached on the virus-injected surface and secured with super glue and Metabond (Parkell) darkened with carbon powder. After 3 weeks of virus expression, a holder (Inscopix, gripper part ID: 1050-002199) was used to lower the miniature microscope (Inscopix, nVista 3.0) with the baseplate onto the top of the GRIN lens until the GCaMP6f fluorescence was visible under the illumination from the miniscope′s light-emitting diode (LED). Subsequently, the baseplate was fixed to the skull with dental cement darkened with carbon powder to prevent external light from contaminating the imaging field of view. A cover (Inscopix, part ID: 1050-002193) was attached to the baseplate to protect the microendoscope.

For wide-field calcium imaging, mice expressing GCaMP7f (injected retro-orbitally with AAV PHP.eB.syn.jGCaMP7f) were anesthetized with isoflurane (4% induction and 2% maintenance). The scalp and the periosteum were removed, and the skull surface and wound margins were covered with Vetbond. Layers of UV-curing optical glue (Norland 81) were applied to reduce light scattering. Metabond was used to secure the wound margins and to attach a metal headpost over the interparietal bone.

### Intrinsic signal optical imaging

Mice were anesthetized with isoflurane (3% induction and 0.7% maintenance), and the whiskers on the left pad, except C2 whisker, were trimmed before starting the intrinsic imaging. A tube for the air puff connected to a Picospritzer (Parker) was positioned next to the left C2 whisker. Images were acquired using a Basler ace acA1920-155 μm camera with a macroscope composed of 50- and 35-mm lens. The cortical surface blood vessels were visualized through the intact bone covered with UV-curing optical adhesive. An initial image was taken of the cortical vasculature under green light (525 nm) to enable alignment of intrinsic signal images with surface vessels. Then, the camera was focused down below the surface (~500 μm). The green light was switched to red 630-nm light for functional imaging, and then the images (480 × 300 pixels, 8 mm × 5 mm) were acquired at 10 frames per second (fps) using the custom-written LabView software (National Instruments, TX). Air puff stimuli delivered to the C2 whisker were applied at 6 Hz for 4 s, and the intrinsic signal was quantified as the difference in the reflected light during stimulus compared to that immediately before. C2 barrel responses were aligned to the blood vessel pattern to guide the surgery for the craniotomy and viral injection.

### Wide-field calcium imaging

Mice were head-fixed on a treadmill, and their dorsal cortex was imaged during laser stimulation ($n$ = 6 mice; wavelength, 1450 nm; power, 300 mW; beam diameter, ~1 mm; pulse duration, 75 to 300 ms; 15-s interstimulus interval; and 20 repetitions per pulse duration) and von Frey stimulation ($n$ = 5 mice; intensity, 0.04 to 1 g; 1-s duration; 12- to 16-s interstimulus interval; 40 repetitions per von Frey intensity). Images were acquired by a PCO.edge 4.2 camera (40 fps, 15 ms all lines exposure time, and 500 × 500 pixels, 13 × 13 mm) mounted on a tandem-lens epifluorescence macroscope (front lens, Canon 85 mm F1.8; back lens, Nikkor 105 mm F2). The cortex was illuminated by alternating 405- and 475-nm illumination at 20 Hz. GCaMP fluorescence was filtered by a 495-nm dichroic mirror (Chroma T495lpxr-UF2) and a band-pass emission filter (Chroma ET525/50m). Rescaled $dF/F_0$ responses measured at 405 nm were subtracted from the $dF/F_0$ responses measured at 475 nm to correct for hemodynamic artefacts (*69*, *70*). We simultaneously recorded behavior by illuminating the animal with infrared light and capturing frames at 200 fps using a Basler acA720-520 μm mounted with a UV-visible cutoff filter (Edmund optics). Synchronization of LEDs, video frame exposure, and stimulus timing were controlled by an Arduino microcontroller, using the PCO camera transistor-transistor logic (TTLs) as a master clock. Behavior video frames were recorded with Bonsai (bonsai-rx.org). Wipe trials were identified using DeepLabCut (*71*). For each animal, we identified the thresholds for noxious laser and von Frey stimulation as the pulse duration and the von Frey intensity, which elicited wipes on ~50% of the trials. The activity maps presented in this study (Fig. 2, C and E, and fig. S4) were measured at these individual thresholds, and consequently, the population responses in Fig. 2 (D and F) average responses to different stimuli. The position of the barrel cortex was determined in separate experiments by mapping the responses to the stimulation of individual whiskers.

### Histology

Animals were deeply anesthetized with isoflurane and then transcardially perfused with precooled phosphate-buffered saline (PBS), followed by 4% precooled paraformaldehyde (PFA) fixation solution.

#### *For checking the virus expression in the VPM*

Whole brains were removed, postfixed in 4% PFA overnight at 4°C, cryoprotected in 30% sucrose for 2 to 3 days, and frozen in O.C.T. compound (Tissue-Tek, Sakura). Then, 80-μm coronal brain slices were sectioned using a cryostat. Brain slices were rinsed with PBS between steps, stained with 4′,6-diamidino-2-phenylindole (DAPI; Sigma-Aldrich, D9542) for 1 hour, and then mounted on the slides for taking confocal images.

#### *For checking the virus expression in the S1 barrel*

Whole brains were removed, and the cerebral cortex was carefully dissected away from the rest of the brain, flattened, and fixed between two slides with 2-mm double-sided tape. The whole slides were postfixed in 4% PFA overnight at 4°C, cryoprotected in 30% sucrose for 2 to 3 days, and frozen in O.C.T compound (Tissue-Tek, Sakura). Then, 80-μm horizontal sections were cut

from the flattened brains using the cryostat. Sections were rinsed with PBS between steps, incubated with primary antibody anti-VGluT2 (Millipore, AB2251-I) overnight at 4°C, incubated with secondary antibody Alexa Fluor 647 AffiniPure donkey anti-guinea pig (Jackson ImmunoResearch Laboratories, 706-605-148)/DAPI overnight at 4°C, washed with PBS, and mounted on the slides for taking the confocal images. The original confocal images from the same brain cortex included different barrel units, so they were reconstructed and overlapped in Photoshop based on their conjunction and structure. Last, the stacked image showed the virus expression on the complete barrel cortex.

## Behavior experiments

Mice underwent behavioral testing sessions with full whiskers and tested again in no-whisker (whiskers were trimmed 1 day before testing) sessions. Mice with headposts were adapted on the running wheel for 2 to 3 days before the start of the full-whisker sessions. After the full-whisker sessions were completed, the whiskers (ipsilateral or bilateral) of the mice were trimmed. The mice were then adapted on the running wheel after recovery on the same day, followed by the no-whisker testing sessions starting the next day. For the experimental sessions, we applied air puff and/or radiant heat and von Frey filaments to the mouse whisker pad. For the air puff experiment, we manually applied the air using a blaster, which typically lasted up to 1 s. For the heat experiment, we used the digital controlled halogen lamp with various percentages of the max intensities and either 4- or 5-s stimulus delivery period (Plantar Test, Hargreaves method, IITC Life Science). We tuned the experimental intensity range covering from no nocifensive to full nocifensive behavior from the mice. For the von Frey experiment (Semmes-Weinstein Von Frey, Stoelting), we also used various grades of filaments (0.02 to 0.4 g). The intertrial intervals for all the experiments were all between 20 and 30 s.

### *Initial behavior experiment in Fig. 1*

We only tested the stimuli with full whiskers, contralateral whiskers, and no whiskers. The heat intensities we used were 10, 15, and 20% of the maximum intensity of the halogen lamp, and the von Frey filaments were 0.02, 0.04, 0.07, 0.16, and 0.4 g. For each intensity, we repeated the trials 10 to 20 times on $n = 13$ (5 male and 8 female mice, for both full-whisker and no-whisker experiments) C57BL/6J mice and $n = 7$ (3 male and 4 female mice, for contralateral whiskers experiment) C57BL/6J mice.

### *Fiber photometry experiment in Fig. 3*

Fiber photometry recording (RWD) was used to record the population calcium fluorescence from the $VPM_{Ntng1}$ neurons. We applied both innocuous and noxious stimuli with full whiskers. We chose the optimal intensity for the noxious stimuli (heat 15%, von Frey 0.4 g) that elicited nocifensive behaviors and also allowed whisking-induced analgesia. Individual stimuli were repeatedly applied 10 to 20 trials on the whisker pad of $VPM_{Ntng1\text{-}GCaMP6m}$ mice ($n = 6$), and video and calcium signals were simultaneously recorded.

### *Manipulation experiment in Fig. 4*

We applied stimuli with full whiskers. The heat intensities we used were 10, 15, and 20%, and the von Frey filaments were 0.07, 0.16, and 0.4 g. We repeated the trials 10 to 20 times on the whisker pad of $VPM_{Ntng1\text{-}PSAM}$ mice ($n = 8$). For each stimulus type per mouse, we conducted a pre- and post-drug session as baseline controls, in addition to the PSEM308 session, which blocks the $VPM_{Ntng1}$ input signals to S1.

### *Calcium imaging experiment in Figs. 5 and 6*

We used Inscopix nVista3.0 system to record the calcium dynamics from the neuronal population of S1B L2/3. The frame rate of all the sessions was 20 fps. We applied both innocuous and noxious stimuli with both full whiskers and no whiskers. Again, we chose the optimal intensity for the noxious stimuli (heat 15% and von Frey 0.4 g) that elicited nocifensive behaviors and also allowed the whisking-induced analgesia. For each intensity, we repeated the trials ~30 times (innocuous), and 60 to 120 times (noxious) on C57 mice ($n = 6$), and recorded the calcium signals of L2/3 neurons of S1B C2 and neighboring barrels.

## Behavioral data analysis

All behavior videos were manually processed. We tracked stimulus onset moments, whisking periods, and wiping moments throughout the whole video. Specifically, stimulus onset and whisking on/off moments were tracked precisely to a single frame, and for the wiping, each time the paw touching the whiskers/face was considered as a wiping moment. For the no-whisker trials, we labeled the whisking periods based on mice facial muscle movement. In addition, throughout the experiments, we found that the coupling between the mouse whisking and running was high. The tracked factors were then converted into binary labeling, indicating the framewise on and off of each factor. Moreover, to include the potential lasting effect of the stimulus and wiping, a duration of effect was assigned to each stimulus onset and wiping moments. For air puff and von Frey (often with a single wiping) trials, the duration of effect was 2 s, while for heat trials, the duration was 5 s.

For the behavioral analysis (initial behavior in Fig. 1 and $VPM_{Ntng1}$ chemical slicing experiment in Fig. 3), two measures—wiping numbers (how many times a mouse wiped the face during a trial) and wiping trial percentage—were used to characterize the level of the nocifensive behavior. The mean and SE were calculated by the wiping number of all the trials, while the wiping trial percentage was calculated by that of the individual mice.

## Fiber photometry data analysis

### *Signal preprocessing*

The 470-nm signal was baseline-corrected by the 410-nm channel, and photobleaching was corrected by adaptive baseline estimation custom written in MATLAB. For the baseline estimation, the signal was first cleaned using wavelet signal denoising. Then, the key turning points were extracted by Ramer-Douglas-Peucker algorithm (*72*, *73*), followed by adaptive thresholding (see below) to find the key turning points representing the baseline dynamics. The baseline was then estimated by piecewise linear interpolation using the key baseline turning points.

### *Factor-related signal extraction*

We assume that the factor-related signals follow the rule of linear superposition. The signal was first converted to deconvolved calcium signal space using constrained foopsi (*47*). The deconvolved calcium signal could be considered as rescaled overall calcium influx from the neural population that was being recorded. Then, all the labeling we extracted from the behavior videos for the three factors, stimulus (either air puff, heat, or von Frey), whisking, and wiping, was combined to be a threefold factor labeling (the factors of stimulus, including air puff, von Frey, and wiping, were

attached with a window of ~1 s to include the potential lasting activity), e.g., [1, 1, 0], indicating that this frame contains stimulus, whisking, but not wiping. Each frame belonged to one of the $2^3 = 8$ conditions. To extract one factor-related signal, we first collected all the calcium imaging frames with this factor labeling being 1, and then pooled frames based on the type of the labeling, for example, [1, 1, 0], [1, 0, 0], [1, 0, 1], and [1, 1, 1] are types of conditions containing the stimulus factor. For each condition, we calculated the intensity distribution of the deconvolved signal and then calculated the distribution of the corresponding factor-negative conditions, for example, [0, 1, 0] and [0, 0, 0], [0, 0, 1] and [0, 1, 1] for the above example. By assumption, the distribution difference between conditions only differing in the presence or absence of the factor of interest could be approximately ascribed to the pure factor–related signal. After calculating the factor-related distribution, we then applied a randomized event pick procedure to generate the pure factor–related deconvolved signal. For each intensity subrange of the distribution, we randomly selected the number of frames based on the factor-related distribution whose deconvolved signals were falling within the subrange. We repeated this process multiple times ($n = 100$) and then computed the average of the realizations. This average was then considered as the pure factor–related deconvolved signal. We applied the method to whisking and wiping separately and generated the stimulus-related factor by calculating the residual of subtracting the above two signals from the raw signal to compensate for the fewer time points for the stimulus factor. To calculate the fluorescence signal, the deconvolved signal was then convolved using the same parameters of the autoregressive process.

## In vivo calcium imaging data analysis

### *Calcium data processing*

The calcium imaging data were processed using MIN1PIPE (*49*). The factor-related signal extraction described above for fiber photometry was extended to multichannel calcium imaging data by picking events from multichannel signals instead of the same single channel, and all three factors were estimated by the method. Post-processing manual ROI selection was conducted to remove any non–neuron-like ROIs before any analyses, independent of the analysis procedures. For a single behavioral configuration, the combination of key factors of interest such as stimulus, whisking, and wiping, we pooled the data from that configuration into a data tensor of the dimensions of neuron number, length of a trial, and trial number. For different average measures, we operated along corresponding dimensions.

### *Calcium data analysis*

To extract active neurons or trials, we adaptively calculated the threshold based on each neurons' $n$ times ($n = 1$ or 2) of SD. For active neuron ratio, a neuron is considered active during the trial if it had at least one calcium event larger than 1 SD of the signal in each trial (trial duration, 5 s for heat and 2 s for von Frey). For active trial percentage of a given neuron, the threshold was defined by 1 SD of the maximum intensity of all trials for that neuron. By this criterion, if a neuron has background activity, and if the stimulus did not increase its calcium signals in a trial, then the neuron is not considered having an active trial.

### *Same-cell tracking (across sessions/days analysis)*

To track the same neurons across all sessions, we applied modified CellReg (*50*) on all the sessions of the same mouse. Because a direct tracking using one of the sessions as the reference would increase the missing rate when the target session was far apart from the reference, we thus tracked the same neurons in a cyclic repeating pattern. In each repetition, a different session served as the reference session on which other sessions were registered. We first extracted the maximal number of trackable neurons to be the minimum of the maximum neuron number from each repetition. Then, for each neuron, the corresponding neuron identity was extracted for each repetition, and the final correspondence was set to be the mode of all the individual corresponding identities.

### *Tensor component analysis*

We applied the TCA (*52*, *74*) on the fluorescence data tensor to decompose the tensor into individual components. To identify neural correlates of S1B activity with facial nociception, we focused on the collective feature of a group of components, rather than individual components to reduce the potential bias. Specifically, we assigned a large number of expected components to improve the fitting performance ($n = 80$). We also ran the modeling for each session multiple times ($n = 50$), and then the decomposed trial factors of all the components were compared with the real behavior factor readouts (i.e., whisking, no-whisking, wiping, and no-wiping), and a cosine similarity was computed for each of them. The first $m = 4$ components with the top similarity were extracted from each mouse and formed a matrix of behavior-relevant components of size 24. Because in TCA there is no unique scale information in the decomposition, we thus normalized all the components for the downstream analyses. To calculate the weighted temporal factor for subclusters focusing on pain versus no pain sensed (i.e., wiping versus no wiping responses), we first divided the temporal domain into 1-s bins and focused only on the bin containing the neural dynamics right before the wiping behavior ([2, 3 s] for heat and [0, 1 s] for von Frey). Then, we extracted the temporal factors from the matrix of behavior-relevant components whose rising phase (for heat; peak for von Frey due to the rapid wiping behavior after stimulus application) fell within the bin range, and computed the average of these factors with the scale of the percentage of the factors in this bin.

### *S1B activity manifold analysis*

A manifold of the S1B activity was learned for each session. First, we formed the data matrix of that session using the deconvolved calcium signal, which was an $n \times T$ matrix, where $n$ is the number of neurons and $T$ is the number of time points. The data matrix was then binarized through thresholding using 1 SD of each trace, and time points with all zero elements were excluded (*75*). To estimate the intrinsic dimension of the manifold, we applied PCA on the data matrices and considered the first $n$ dimensions whose cumulative variance explained by the $n$ dimensions exceeded 97.5% (fig. S7) (*54*). A manifold learning algorithm, Laplacian Eigenmap, was then applied to the data matrix (*53*), with $d = 10$ as the dimension of the embeddings, used based on the initial estimation of the intrinsic dimensions. An adjacency matrix was first constructed by computing the nearest neighbors ($P = 0.25\%$ for the first iteration and $P = 10\%$ for the second iteration) (*75*). Then, a weight matrix was constructed using the parameter-free method based on the adjacency matrix (*53*). The problem of manifold learning was then converted to solving an eigenvalue problem. The learned manifold was usually spatially distorted, resulting in the failure of preserving the geometry of the data. Therefore, we applied Megaman (*56*) to recover the geometric

information of the learned embedding. The metric learned applied to any pairs of points on the embedded manifold.

To further estimate the embeddings of the subspaces for different behavioral configurations, we applied PCA and preserved the first dimensions, which explained 99% variance in total. To extract the shared dimensions between two subspaces, we applied a method using basic linear operations, given the bases vectors of the two input subspaces. To calculate the trajectory length along the embedded manifold, we converted the embedded manifold to an undirected graph, with the distance between pairs of points to be corrected by the learned metric. Then, for any neighboring two temporal points along the trajectory, we computed the shortest path (Dijkstra's algorithm) (*76*) on the graph and calculated the distance of this shortest path, as the approximation of the geodesic length on the manifold. To finally get the trajectory length, we summed up the distances of all the neighboring temporal points along the trajectory within a trial computed in the above way.

### Statistics

All statistical analyses were performed in MATLAB (MathWorks). Unless mentioned explicitly, most behavior data, including the full whiskers, contralateral whiskers, and no whiskers behavioral experiments (with or without whisking), were tested with repeated-measures ANOVA and two-tailed paired *t* test. Normality test using Anderson-Darling test was performed for the main behavior data. Because comparison between Friedman's test and repeated-measures ANOVA revealed no major difference between the two tests on our data, we only reported results of repeated-measures ANOVA. Fiber photometry data were tested with two-tailed two-sample *t* test. Manipulation experiments and wide-field imaging data were tested with one-way repeated-measures ANOVA, where the former was also tested with post hoc Tukey's honestly significant difference examination between pairs of conditions. Further linear mixed-effect model was applied to both heat and von Frey experiments, where there was no strong significance due to the information loss at computing the mouse average for ANOVA. Significance levels are indicated as follows: $^{*}P < 0.025$, $^{**}P < 0.01$, $^{***}P < 1 \times 10^{-4}$, and $^{****}P < 1 \times 10^{-6}$. All graphs contain individual data points and means ± SEM.

## Supplementary Materials

**This PDF file includes:**
Figs. S1 to S10

**Other Supplementary Material for this manuscript includes the following:**
Movies S1 and S2

View/request a protocol for this paper from *Bio-protocol*.

## REFERENCES AND NOTES


1. R. Melzack, P. D. Wall, Pain mechanisms: A new theory. *Science* **150**, 971–979 (1965).
2. M. W. Salter, J. L. Henry, Differential responses of nociceptive vs. non-nociceptive spinal dorsal horn neurones to cutaneously applied vibration in the cat. *Pain* **40**, 311–322 (1990).
3. M. W. Salter, J. L. Henry, Physiological characteristics of responses of wide dynamic range spinal neurones to cutaneously applied vibration in the cat. *Brain Res.* **507**, 69–84 (1990).
4. D. Le Bars, The whole body receptive field of dorsal horn multireceptive neurones. *Brain Res. Rev.* **40**, 29–44 (2002).
5. C. Zampino, R. Ficacci, M. Checcacci, F. Franciolini, L. Catacuzzeno, Pain control by proprioceptive and exteroceptive stimulation at the trigeminal level. *Front. Physiol.* **9**, 1037 (2018).
6. F. Mancini, T. Nash, G. D. Iannetti, P. Haggard, Pain relief by touch: A quantitative approach. *Pain* **155**, 635–642 (2014).
7. K. Inui, T. Tsuji, R. Kakigi, Temporal analysis of cortical mechanisms for pain relief by tactile stimuli in humans. *Cereb. Cortex* **16**, 355–365 (2006).
8. F. Mancini, A.-L. Beaumont, L. Hu, P. Haggard, G. D. D. Iannetti, Touch inhibits subcortical and cortical nociceptive responses. *Pain* **156**, 1936–1944 (2015).
9. H. Nahra, L. Plaghki, Modulation of perception and neurophysiological correlates of brief $CO_2$ laser stimuli in humans using concurrent large fiber stimulation. *Somatosens. Mot. Res.* **20**, 139–147 (2003).
10. C. J. Vierck, B. L. Whitsel, O. V. Favorov, A. W. Brown, M. Tommerdahl, Role of primary somatosensory cortex in the coding of pain. *Pain* **154**, 334–344 (2013).
11. M. C. Bushnell, G. H. Duncan, R. K. Hofbauer, B. Ha, J. I. Chen, B. Carrier, Pain perception: Is there a role for primary somatosensory cortex? *Proc. Natl. Acad. Sci. U.S.A.* **96**, 7705–7709 (1999).
12. M. Gamal-Eltrabily, G. Martínez-Lorenzana, A. González-Hernández, M. Condés-Lara, Cortical modulation of nociception. *Neuroscience* **458**, 256–270 (2021).
13. A. Mouraux, G. D. Iannetti, The search for pain biomarkers in the human brain. *Brain* **141**, 3290–3307 (2018).
14. K. H. Brodersen, K. Wiech, E. I. Lomakina, C.-S. Lin, J. M. Buhmann, U. Bingel, M. Ploner, K. E. Stephan, I. Tracey, Decoding the perception of pain from fMRI using multivariate pattern analysis. *Neuroimage* **63**, 1162–1170 (2012).
15. E. A. Moulton, G. Pendse, L. R. Becerra, D. Borsook, BOLD responses in somatosensory cortices better reflect heat sensation than pain. *J. Neurosci.* **32**, 6024–6031 (2012).
16. M. Ploner, J. Gross, L. Timmermann, A. Schnitzler, Cortical representation of first and second pain sensation in humans. *Proc. Natl. Acad. Sci. U.S.A.* **99**, 12444–12448 (2002).
17. N. Forss, T. T. Raij, M. Seppä, R. Hari, Common cortical network for first and second pain. *Neuroimage* **24**, 132–142 (2005).
18. R. M. S. Panchuelo, S. Eldeghaidy, A. Marshall, F. McGlone, S. T. Francis, O. Favorov, A nociresponsive specific area of human somatosensory cortex within BA3a: BA3c? *Neuroimage* **221**, 117187 (2020).
19. Z. G. Zhang, L. Hu, Y. S. Hung, A. Mouraux, G. D. Iannetti, Gamma-band oscillations in the primary somatosensory cortex—A direct and obligatory correlate of subjective pain intensity. *J. Neurosci.* **32**, 7429–7438 (2012).
20. L. M. Chen, R. M. Friedman, A. W. Roe, Area-specific representation of mechanical nociceptive stimuli within SI cortex of squirrel monkeys. *Pain* **141**, 258–268 (2009).
21. O. V. Favorov, V. Pellicer-Morata, A. L. DeJongh Curry, J. T. Ramshur, A. Brna, T. D. Challener, R. S. Waters, A newly identified nociresponsive region in the transitional zone (TZ) in rat sensorimotor cortex. *Brain Res.* **1717**, 228–234 (2019).
22. L. L. Tan, M. J. Oswald, C. Heinl, O. A. Retana Romero, S. K. Kaushalya, H. Monyer, R. Kuner, Gamma oscillations in somatosensory cortex recruit prefrontal and descending serotonergic pathways in aversion and nociception. *Nat. Commun.* **10**, 983 (2019).
23. L. Yue, G. D. Iannetti, L. Hu, The neural origin of nociceptive-induced gamma-band oscillations. *J. Neurosci.* **40**, 3478–3490 (2020).
24. J. Cichon, T. J. J. Blanck, W. B. Gan, G. Yang, Activation of cortical somatostatin interneurons prevents the development of neuropathic pain. *Nat. Neurosci.* **20**, 1122–1132 (2017).
25. Y. Liu, A. Latremoliere, X. Li, Z. Zhang, M. Chen, X. Wang, C. Fang, J. Zhu, C. Alexandre, Z. Gao, B. Chen, X. Ding, J.-Y. Zhou, Y. Zhang, C. Chen, K. H. Wang, C. J. Woolf, Z. He, Touch and tactile neuropathic pain sensitivity are set by corticospinal projections. *Nature* **561**, 547–550 (2018).
26. C. C. H. Petersen, Sensorimotor processing in the rodent barrel cortex. *Nat. Rev. Neurosci.* **20**, 533–546 (2019).
27. M. E. Diamond, M. von Heimendahl, P. M. Knutsen, D. Kleinfeld, E. Ahissar, 'Where' and 'what' in the whisker sensorimotor system. *Nat. Rev. Neurosci.* **9**, 601–612 (2008).
28. D. Kleinfeld, M. Deschênes, Neuronal basis for object location in the vibrissa scanning sensorimotor system. *Neuron* **72**, 455–468 (2011).
29. J. Yu, D. A. Gutnisky, S. A. Hires, K. Svoboda, Layer 4 fast-spiking interneurons filter thalamocortical signals during active somatosensation. *Nat. Neurosci.* **19**, 1647–1657 (2016).
30. L. J. Gentet, M. Avermann, F. Matyas, J. F. Staiger, C. C. H. Petersen, Membrane potential dynamics of GABAergic neurons in the barrel cortex of behaving mice. *Neuron* **65**, 422–435 (2010).
31. J. C. Curtis, D. Kleinfeld, Phase-to-rate transformations encode touch in cortical neurons of a scanning sensorimotor system. *Nat. Neurosci.* **12**, 492–501 (2009).
32. D. H. O'Connor, S. P. Peron, D. Huber, K. Svoboda, Neural activity in barrel cortex underlying vibrissa-based object localization in mice. *Neuron* **67**, 1048–1061 (2010).
33. S. P. Jadhav, J. Wolfe, D. E. Feldman, Sparse temporal coding of elementary tactile features during active whisker sensation. *Nat. Neurosci.* **12**, 792–800 (2009).

34. L. W. Bosman, A. R. Houweling, C. B. Owens, N. Tanke, O. T. Shevchouk, N. Rahmati, W. H. Teunissen, C. Ju, W. Gong, S. K. E. Koekkoek, C. I. De Zeeuw, Anatomical pathways involved in generating and sensing rhythmic whisker movements. *Front. Integr. Neurosci.* **5**, 53 (2011).
35. B. S. Sermet, P. Truschow, M. Feyerabend, J. M. Mayrhofer, T. B. Oram, O. Yizhar, J. F. Staiger, C. C. Petersen, Pathway-, layer- and cell-type-specific thalamic input to mouse barrel cortex. *eLife* **8**, e52665 (2019).
36. P. Bokiniec, N. Zampieri, G. R. Lewin, J. F. Poulet, The neural circuits of thermal perception. *Curr. Opin. Neurobiol.* **52**, 98–106 (2018).
37. C. Gauriau, J.-F. Bernard, A comparative reappraisal of projections from the superficial laminae of the dorsal horn in the rat: The forebrain. *J. Comp. Neurol.* **468**, 24–56 (2004).
38. C. Condylis, E. Lowet, J. Ni, K. Bistrong, T. Ouellette, N. Josephs, J. L. Chen, Context-dependent sensory processing across primary and secondary somatosensory cortex. *Neuron* **106**, 515–525.e5 (2020).
39. E. Welker, P. V. Hoogland, H. Van der Loos, Organization of feedback and feedforward projections of the barrel cortex: A PHA-L study in the mouse. *Exp. Brain Res.* **73**, 411–435 (1988).
40. L. A. DeNardo, D. S. Berns, K. DeLoach, L. Luo, Connectivity of mouse somatosensory and prefrontal cortex examined with trans-synaptic tracing. *Nat. Neurosci.* **18**, 1687–1697 (2015).
41. D. A. Gehrlach, C. Weiand, T. N. Gaitanos, E. Cho, A. S. Klein, A. A. Hennrich, K.-K. Conzelmann, N. Gogolla, A whole-brain connectivity map of mouse insular cortex. *eLife* **9**, e55585 (2020).
42. G. Minamisawa, S. E. Kwon, M. Chevée, S. P. Brown, D. H. O'Connor, A non-canonical feedback circuit for rapid interactions between somatosensory cortices. *Cell Rep.* **23**, 2718–2731.e6 (2018).
43. G. Hafner, M. Witte, J. Guy, N. Subhashini, L. E. Fenno, C. Ramakrishnan, Y. S. Kim, K. Deisseroth, E. M. Callaway, M. Oberhuber, K.-K. Conzelmann, J. F. Staiger, Mapping brain-wide afferent inputs of Parvalbumin-expressing GABAergic neurons in barrel cortex reveals local and long-range circuit motifs. *Cell Rep.* **28**, 3450–3461.e8 (2019).
44. S. E. Kwon, H. Yang, G. Minamisawa, D. H. O'Connor, Sensory and decision-related activity propagate in a cortical feedback loop during touch perception. *Nat. Neurosci.* **19**, 1243–1249 (2016).
45. K. A. Bolding, S. Nagappan, B.-X. Han, F. Wang, K. M. Franks, Recurrent circuitry is required to stabilize piriform cortex odor representations across brain states. *eLife* **9**, e53125 (2020).
46. J. C. Lin, W.-H. Ho, A. Gurney, A. Rosenthal, The netrin-G1 ligand NGL-1 promotes the outgrowth of thalamocortical axons. *Nat. Neurosci.* **6**, 1270–1276 (2003).
47. E. A. Pnevmatikakis, D. Soudry, Y. Gao, T. A. Machado, J. Merel, D. Pfau, T. Reardon, Y. Mu, C. Lacefield, W. Yang, M. Ahrens, R. Bruno, T. M. Jessell, D. S. Peterka, R. Yuste, L. Paninski, Simultaneous denoising, deconvolution, and demixing of calcium imaging data. *Neuron* **89**, 285–299 (2016).
48. C. J. Magnus, P. H. Lee, D. Atasoy, H. H. Su, L. L. Looger, S. M. Sternson, Chemical and genetic engineering of selective ion channel-ligand interactions. *Science* **333**, 1292–1296 (2011).
49. J. Lu, C. Li, J. Singh-Alvarado, Z. C. Zhou, F. Fröhlich, R. Mooney, F. Wang, MIN1PIPE: A miniscope 1-photon-based calcium imaging signal extraction pipeline. *Cell Rep.* **23**, 3673–3684 (2018).
50. L. Sheintuch, A. Rubin, N. Brande-Eilat, N. Geva, N. Sadeh, O. Pinchasof, Y. Ziv, Tracking the same neurons across multiple days in $Ca^{2+}$ imaging data. *Cell Rep.* **21**, 1102–1115 (2017).
51. S. Crochet, J. F. Poulet, Y. Kremer, C. C. H. Petersen, Synaptic mechanisms underlying sparse coding of active touch. *Neuron* **69**, 1160–1175 (2011).
52. A. H. Williams, T. H. Kim, F. Wang, S. Vyas, S. I. Ryu, K. V. Shenoy, M. Schnitzer, T. G. Kolda, S. Ganguli, Unsupervised discovery of demixed, low-dimensional neural dynamics across multiple timescales through tensor component analysis. *Neuron* **98**, 1099–1115.e8 (2018).
53. M. Belkin, P. Niyogi, Laplacian eigenmaps for dimensionality reduction and data representation. *Neural Comput.* **15**, 1373–1396 (2003).
54. L. Van Der Maaten, E. Postma, J. van den Herik, Dimensionality reduction: A comparative. *J. Mach. Learn. Res.* **10**, 13 (2009).
55. D. Perraul-Joncas, M. Meilă, Non-linear dimensionality reduction: Riemannian metric estimation and the problem of geometric discovery. arXiv:1305.7255 [stat.ML] (30 May 2013).
56. J. McQueen, M. Meilă, J. VanderPlas, Z. Zhang, Megaman: Scalable manifold learning in python. *J. Mach. Learn. Res.* **17**, 5176–5180 (2016).
57. U. Bauer, Ripser: Efficient computation of Vietoris–Rips persistence barcodes. *J. Appl. Comput. Topol.* **5**, 391–423 (2021).
58. Z. V. Guo, N. Li, D. Huber, E. Ophir, D. Gutnisky, J. T. Ting, G. Feng, K. Svoboda, Flow of cortical activity underlying a tactile decision in mice. *Neuron* **81**, 179–194 (2014).
59. H. Yang, S. E. Kwon, K. S. Severson, D. H. O'Connor, Origins of choice-related activity in mouse somatosensory cortex. *Nat. Neurosci.* **19**, 127–134 (2016).
60. S. Musall, M. T. Kaufman, A. L. Juavinett, S. Gluf, A. K. Churchland, Single-trial neural dynamics are dominated by richly varied movements. *Nat. Neurosci.* **22**, 1677–1686 (2019).
61. C. Stringer, M. Pachitariu, N. Steinmetz, C. B. Reddy, M. Carandini, K. D. Harris, Spontaneous behaviors drive multidimensional, brainwide activity. *Science* **364**, 255 (2019).
62. N. A. Steinmetz, P. Zatka-Haas, M. Carandini, K. D. Harris, Distributed coding of choice, action and engagement across the mouse brain. *Nature* **576**, 266–273 (2019).
63. M. Frot, M. Magnin, F. Mauguiere, L. Garcia-Larrea, Human SII and posterior insula differently encode thermal laser stimuli. *Cereb. Cortex* **17**, 610–620 (2007).
64. N. Milenkovic, W. J. Zhao, J. Walcher, T. Albert, J. Siemens, G. R. Lewin, J. F. Poulet, A somatosensory circuit for cooling perception in mice. *Nat. Neurosci.* **17**, 1560–1566 (2014).
65. L. Hu, G. D. Iannetti, Neural indicators of perceptual variability of pain across species. *Proc. Natl. Acad. Sci. U.S.A.* **116**, 1782–1791 (2019).
66. T. Hua, B. Chen, D. Lu, K. Sakurai, S. Zhao, B. X. Han, J. Kim, L. Yin, Y. Chen, J. Lu, F. Wang, General anesthetics activate a potent central pain-suppression circuit in the amygdala. *Nat. Neurosci.* **23**, 854–868 (2020).
67. M. M. Heinricher, Pain modulation and the transition from acute to chronic pain. *Adv. Exp. Med. Biol.* **904**, 105–115 (2016).
68. S. Hirschberg, Y. Li, A. Randall, E. J. Kremer, A. E. Pickering, Functional dichotomy in spinal- vs prefrontal-projecting locus coeruleus modules splits descending noradrenergic analgesia from ascending aversion and anxiety in rats. *eLife* **6**, (2017).
69. J. B. Wekselblatt, E. D. Flister, D. M. Piscopo, C. M. Niell, Large-scale imaging of cortical dynamics during sensory perception and behavior. *J. Neurophysiol.* **115**, 2852–2866 (2016).
70. W. E. Allen, I. V. Kauvar, M. Z. Chen, E. B. Richman, S. J. Yang, K. Chan, V. Gradinaru, B. E. Deverman, L. Luo, K. Deisseroth, Global representations of goal-directed behavior in distinct cell types of mouse neocortex. *Neuron* **94**, 891–907.e6 (2017).
71. A. Mathis, P. Mamidanna, K. M. Cury, T. Abe, V. N. Murthy, M. W. Mathis, M. Bethge, DeepLabCut: Markerless pose estimation of user-defined body parts with deep learning. *Nat. Neurosci.* **21**, 1281–1289 (2018).
72. U. Ramer, An iterative procedure for the polygonal approximation of plane curves. *Comput. Graph. Image Process.* **1**, 244–256 (1972).
73. D. H. Douglas, T. K. Peucker, Algorithms for the reduction of the number of points required to represent a digitized line or its caricature. *Cartographica* **10**, 112–122 (1973).
74. J. Kim, H. Park, Fast nonnegative matrix factorization: An active-set-like method and comparisons. *SIAM J. Sci. Comput.* **33**, 3261–3281 (2011).
75. A. Rubin, L. Sheintuch, N. Brande-Eilat, O. Pinchasof, Y. Rechavi, N. Geva, Y. Ziv, Revealing neural correlates of behavior without behavioral measurements. *Nat. Commun.* **10**, 4745 (2019).
76. E. W. Dijkstra, A note on two problems in connexion with graphs. *Numer. Math.* **1**, 269–271 (1959).


**Acknowledgments:** We thank T. Hua for the initial help with the von Frey experiment and J. Park for help with the fiber photometry. **Funding:** This work was supported by NIH grant NS109947, a subproject to NIH grant P01-AT009968. **Author contributions:** F.W. conceived and supervised the project. F.W., J.L., and B.C. designed the experiments. B.C. and J.T. performed surgeries and virus injections. J.L., B.C., and P.X. performed behavioral tests. M.L. and V.P. built the wide-field imaging system and performed wide-field imaging. B.C., M.L., and P.M.T. performed intrinsic imaging. J.L. and B.C. performed calcium miniscope imaging. J.L. processed and analyzed the behavioral and neural data. B.-X.H. took care of mouse husbandry and genotyping. Z.H. provided the critical reagents. F.W., J.L., B.C., M.L., and V.P. wrote the manuscript. **Competing interests:** Z.H. is a consultant for SpineX and Myro Therapeutics. The authors declare no other competing interests. **Data and materials availability:** All data needed to evaluate the conclusions in the paper are present in the paper and/or the Supplementary Materials, and can be found in https://dataverse.harvard.edu/dataset.xhtml?persistentId=doi:10.7910/DVN/A8SRDN&faces-redirect=true. All major codes used in this study are available from the same dataset including the MINIPIPE code for processing miniscope imaging (correspondence should be addressed to J.L., jinghaol@mit.edu). In addition, MINIPIPE is available at https://github.com/JinghaoLu/MIN1PIPE.

Submitted 10 December 2021
Accepted 20 October 2022
Published 16 November 2022
10.1126/sciadv.abn6530